Quasineutral plasma expansion into infinite vacuum as a model for parallel ELM transport



2013 Plasma Phys. Control. Fusion 55 085003

(http://iopscience.iop.org/0741-3335/55/8/085003)

Plasma Phys. Control. Fusion **55** (2013) 085003 (21pp) doi:10.1088/0741-3335/55/8/085003

# Quasineutral plasma expansion into infinite vacuum as a model for parallel ELM transport

**D Moulton[1], Ph Ghendrih[1], W Fundamenski[2], G Manfredi[3] and D Tskhakaya[4,5]**

[1] CEA-IRFM, F-13108 Saint-Paul-lez-Durance, France
[2] EURATOM/CCFE Fusion Association, Culham Science Centre, Abingdon, Oxfordshire, OX143DB, UK
[3] Institut de Physique et Chimie des Matériaux, CNRS and Université de Strasbourg, BP 43, F-67034 Strasbourg, France
[4] Association EURATOM-ÖAW, University of Innsbruck, A-6020 Innsbruck, Austria

E-mail: david.moulton@cea.fr

Received 16 January 2013, in final form 20 April 2013
Published 21 May 2013
Online at stacks.iop.org/PPCF/55/085003

**Abstract**

An analytic solution for the expansion of a plasma into vacuum is assessed for its relevance to the parallel transport of edge localized mode (ELM) filaments along field lines. This solution solves the 1D1V Vlasov–Poisson equations for the adiabatic (instantaneous source), collisionless expansion of a Gaussian plasma bunch into an infinite space in the quasineutral limit. The quasineutral assumption is found to hold as long as $\lambda_{D0}/\sigma_0 \lesssim 0.01$ (where $\lambda_{D0}$ is the initial Debye length at peak density and $\sigma_0$ is the parallel length of the Gaussian filament), a condition that is physically realistic. The inclusion of a boundary at $x = L$ and consequent formation of a target sheath is found to have a negligible effect when $L/\sigma_0 \gtrsim 5$, a condition that is physically plausible. Under the same condition, the target flux densities predicted by the analytic solution are well approximated by the 'free-streaming' equations used in previous experimental studies, strengthening the notion that these simple equations are physically reasonable. Importantly, the analytic solution predicts a zero heat flux density so that a fluid approach to the problem can be used equally well, at least when the source is instantaneous. It is found that, even for JET-like pedestal parameters, collisions *can* affect the expansion dynamics via electron temperature isotropization, although this is probably a secondary effect. Finally, the effect of a finite duration, $\tau_{src}$, for the plasma source is investigated. As is found for an instantaneous source, when $L/\sigma_0 \gtrsim 5$ the presence of a target sheath has a negligible effect, at least up to the explored range of $\tau_{src} = L/c_s$ (where $c_s$ is the sound speed at the initial temperature).

(Some figures may appear in colour only in the online journal)

## 1. Introduction

### *1.1. Motivation*

Safe exhaust of the energy and particles contained in edge localized modes (ELMs) is a key requirement for the successful operation of future tokamaks employing the high-confinement mode. An ELM originates from a magnetohydrodynamic (MHD) eigenmode on closed field lines, the growth of which is driven by a combination of edge current and radial pressure gradient in regions of unfavourable magnetic curvature (Bécoulet *et al* 2003, Snyder and Wilson 2003). Initially positioned in the vicinity of the outboard pre-ELM pedestal, the eigenmode develops nonlinearly into ∼10–20 separate field-aligned pressure perturbations, called filaments.

After their creation, the filaments become magnetically connected to the targets. How exactly this happens, and whether there is a significant period during which the filament

[5] Permanent address: Andronikashvili Institute of Physics, 0177 Tbilisi, Georgia.

 

is connected to both the pedestal *and* the targets is still a matter of debate (Kirk *et al* 2005, Fundamenski *et al* 2007). Whichever way, once they are connected to the targets, energy and particles are transported primarily in the parallel direction to the divertor targets, causing ∼2–20% of the total plasma energy to be lost (Loarte *et al* 2003). Parallel transport will affect, and may primarily determine, the time duration over which the ELM spreads its energy on the target, $\tau_{\mathrm{ELM}}$. This time is of critical importance since the maximum target temperature rise due to an ELM (which should not exceed the melting point of the divertor tiles) is approximately proportional to $1/\sqrt{\tau_{\mathrm{ELM}}}$ (Loarte *et al* 2007, Jachmich *et al* 2011). It is this parallel transport along open field lines which is the focus of the work presented here.

A range of numerical methods exist to model ELM transport. Generally, it is deemed too computationally costly to model ELMs kinetically in more than one spatial dimension. Thus, kinetic codes such as BIT1 (Tskhakaya *et al* 2008, Tskhakaya *et al* 2009) and VESPA (Manfredi *et al* 2011) (both of which are used in this work) tend to model filament transport in the parallel direction only, while fluid codes such as EDGE2D-EIRENE and JOREK are used to model filament transport in multiple directions (Wiesen *et al* 2011 and Pamela *et al* 2011).

In this paper, a kinetic approach is adopted since the density, temperatures and length scales associated with most ELM filaments on present machines (and certainly those on ITER) are collisionless. Thus, *a priori*, a fluid approach could not be justified. Unfortunately, kinetic codes are often computationally intensive, and it can be difficult to discern the dominant physical effects from the simulation output. Fortunately, however, a relevant *analytic* solution exists which captures the dominant physics simulated numerically. This analytic solution forms the backbone of this paper.

### *1.2. Analytic approach for instantaneous-source expansion*

The analytic solution described here was not derived by the authors. In fact, it resulted from a large body of work carried out in the field of laser-driven thermonuclear fusion (Manfredi *et al* 1993, Dorozhkina and Semenov 1998, Dorozhkina and Semenov 1999, Kovalev *et al* 2002, Kovalev and Bychenkov 2003, Mora 2005). To the authors' knowledge, however, it has not yet been applied to ELM parallel transport. The solution is derived by solving the collisionless Vlasov–Poisson (VP) equations in an *infinite* space and *with* the assumption of a quasineutral plasma. For realistic ELM parameters, it is shown to be well matched to numerical solutions in a *bounded* space and *without* any quasineutral assumption. This agreement is achieved because the majority of the simulated plasma does indeed remain quasineutral throughout the expansion and, critically, because the sheath potential set up at the simulation boundary is negligible when the parallel extent of the initial ELM filament perturbation, $\sigma_0$, is at least ∼5 times shorter than the connection length to the target, $L$. This ratio is plausible for present-day tokamaks and for ITER.

The analytic solution is shown to be a generalized version of the free-streaming model for plasma expansion. Currently, the free-streaming model is the primary analytic tool for modelling the particle and energy flux densities at the targets due to an ELM filament. Originally conceived by Fundamenski *et al* (2006), the model solves the Vlasov equation for ions in the absence of a Coulomb potential. This neglect of the potential means that the ions feel no forces and are simply advected towards the targets at an average speed equal to the ion thermal speed $v_{T_i}$. Despite this seemingly crude approach, the free-streaming equations have proven remarkably successful in reproducing the shape of the target power loads on JET and ASDEX Upgrade (Eich *et al* 2009). In this work, a possible explanation for this agreement is put forward by showing that the shape of the free-streaming equations are actually unchanged by the presence of electrons and a self-consistent Coulomb potential, as long as the same condition holds as is required for the sheath to be negligible, i.e. as long as $L/\sigma_0 \gtrsim 5$. Thus, the physical relevance of the free-streaming equations are fortified.

In order to derive the analytic solution, it must be assumed that the source is instantaneous, which means that its evolution depends only on the initial conditions (a Gaussian density perturbation with parallel extent $\sigma_0$ in this case) and that the total number of particles and energy in an infinite domain is constant. (For an infinite domain, the term 'instantaneous source' is therefore synonymous with 'adiabatic', but for a bounded domain it is not, since energy can be lost through the boundaries.) It is argued in section 5.1.6 that the instantaneous-source case could well be physically relevant. If this is not the case, the effect of a finite source duration must be treated numerically, since the authors are unaware of an appropriate analytic solution. This is carried out using the VESPA code in section 4.9.

### *1.3. Paper overview*

The paper is organized as follows. Section 2 describes the 1D1V VP model used throughout. Section 3 describes the analytic solution to the VP model for an instantaneous, Gaussian shaped density source, in the limit of quasineutrality and a slowly varying current. Numerical results from primarily VESPA but also BIT1 simulations are presented in section 4. In these simulations, various assumptions made in the analytic solution are tested for their effect on the solution. The assumptions tested are (i) quasineutrality, (ii) an infinite domain, (iii) an initially Gaussian density profile, (iv) a collisionless 1V plasma, and (v) an instantaneous source. The challenge of including a background plasma is left for future work. Finally, the results are discussed in section 5 and conclusions are drawn in section 6.

## 2. The VP model

### *2.1. Equations*

In the 1D1V VP model used here, the parallel distribution function $f_\alpha(x, v, t)$ evolves according to the collisionless Vlasov equation:

$$\frac{\partial f_\alpha}{\partial t} + v\frac{\partial f_\alpha}{\partial x} - \frac{q_\alpha}{m_\alpha}\frac{\partial \phi}{\partial x}\frac{\partial f_\alpha}{\partial v} = S_\alpha(x, v, t), \tag{1}$$

where $x$ is the 1D spatial coordinate parallel to the magnetic field, $v$ is the parallel velocity coordinate, $\alpha \in \{\mathrm{e}, \mathrm{i}\}$ is the species index (only two-component plasmas are considered in this work), $q_\alpha \in \{-e, Ze\}$ is the species charge, $m_\alpha$ is the species mass, $\phi(x,t)$ is the Coulomb potential and $S_\alpha$ is the source function. $\phi$ evolves according to the Poisson equation:

$$\frac{\partial^2 \phi}{\partial x^2} = -\frac{e}{\epsilon_0}\left(Zn_\mathrm{i} - n_\mathrm{e}\right), \tag{2}$$

where $n_\alpha(x,t) \equiv \int f_\alpha \, \mathrm{d}v$ is the density of species $\alpha$.

Both bounded ($-L \leqslant x \leqslant L$, where $L$ is the connection length of the magnetic field lines being modelled) and unbounded ($-\infty \leqslant x \leqslant \infty$) parallel coordinate systems will be considered. The assumption of an unbounded space is required in order to derive an exact analytic solution for $f_\alpha$. In the bounded case, the VP model is solved numerically with a boundary condition $f_\alpha(x = \pm L, v, t) = \phi(x = \pm L, t) = 0$. It is emphasized that, since this model is one-dimensional, it can only predict quantities which are averaged over some area in the drift plane (i.e. the plane perpendicular to the magnetic field lines).

### 2.2. Source function

It is assumed throughout that $S_\alpha$ is uniform in time for a duration $\tau_\mathrm{src}$, that it is Gaussian along $x$ and symmetric about $x = 0$, and that the injected particles are Maxwellian with parallel temperature $T_{\alpha 0}$. Thus,

$$S_\alpha(x, v, t) = \frac{n_{\alpha 0}\mathcal{U}(t)}{\sqrt{2\pi}\, v_{T\alpha}} \exp\left(-\frac{x^2}{2\sigma_0^2}\right) \exp\left(-\frac{v^2}{2v_{T\alpha}^2}\right), \tag{3}$$

where $\sigma_0$ is the parallel extent of the source, $v_{T\alpha} \equiv \sqrt{T_{\alpha 0}/m_\alpha}$ is the thermal speed of the injected particles, and $n_{\mathrm{e}0} = Zn_{\mathrm{i}0}$ so that the total charge injected is zero. Also, $\mathcal{U}(t)$ is the uniform distribution function, which sets a constant particle injection rate:

$$\mathcal{U}(t) = \begin{cases} 1/\tau_\mathrm{src} & \text{for } 0 \leqslant t \leqslant \tau_\mathrm{src} \\ 0 & \text{otherwise.} \end{cases} \tag{4}$$

The density $n_{\alpha 0}$ in (3) is the initial peak density for the particular case in which the source is *instantaneous*, i.e. when $\tau_\mathrm{src} \to 0$ (see section 3.1). It is important to recognize that there is no background plasma in this model; the source particles expand into vacuum.

The total number of particles injected (per unit area) over an infinite parallel space is

$$N_{\alpha 0} \equiv \int\!\!\int\!\!\int S_\alpha \mathrm{d}x \, \mathrm{d}v \, \mathrm{d}t = \sqrt{2\pi} n_{\alpha 0}\sigma_0, \tag{5}$$

and the total parallel energy injected (per unit area) is

$$E_{\alpha 0} \equiv \int\!\!\int\!\!\int \frac{1}{2} m_\alpha v^2 S_\alpha \, \mathrm{d}x \, \mathrm{d}v \, \mathrm{d}t = \frac{1}{2} N_{\alpha 0} T_{\alpha 0}. \tag{6}$$

Note that the magnitude of $\mathcal{U}(t)$ has been chosen so that both $N_{\alpha 0}$ and $E_{\alpha 0}$ are independent of $\tau_\mathrm{src}$.

### 2.3. Accounting for gyratory energy

The 1D1V VP model only solves for the *parallel* distribution functions. When the perpendicular distribution functions are required, it is assumed that they are Maxwellian with associated perpendicular temperatures $T_{\alpha 0}^\perp = T_{\alpha 0}$, i.e. that the perpendicular temperatures are the same as the parallel temperatures of the particles when they are injected. Furthermore, it is assumed that there is no interaction between the parallel and perpendicular distribution functions, or between the two perpendicular distribution functions. The perpendicular temperatures therefore remain constant in time and space at a value $T_{\alpha 0}$ (the effect of relaxing this assumption is considered in section 4.8).

## 3. Analytic solution with an instantaneous source

### 3.1. Initial conditions

Imposing an instantaneous source ($\tau_\mathrm{src} \to 0$) is equivalent to setting $S_\alpha = 0$ and imposing an initial condition on $f_\alpha$, such that the initial temperatures are equal to $T_{\alpha 0}$ for all $x$ and the initial densities are Gaussian:

$$n_\alpha\left(x, t = 0\right) = n_{\alpha 0} \exp\left(-\frac{x^2}{2\sigma_0^2}\right). \tag{7}$$

It is emphasized that, for the analytic solution, the expansion is into an infinite space, $-\infty \leqslant x \leqslant \infty$, i.e. the effect of a boundary is not accounted for. Note that, as mentioned in the previous section, $n_{\alpha 0}$ is the initial peak density for an instantaneous source. As previously shown by Dorozhkina and Semenov (1998), under these conditions the solution to the VP model is analytically tractable.

### 3.2. The solution

Subtracting the ion and electron momentum balance equations and rearranging yields

$$e\frac{\partial \phi}{\partial x} = \frac{m_\mathrm{e} m_\mathrm{i}}{Z^2 m_\mathrm{e} n_\mathrm{i} + m_\mathrm{i} n_\mathrm{e}} \left(\frac{1}{e}\frac{\partial j}{\partial t} + \frac{\partial}{\partial x}\int v^2 \left(Zf_\mathrm{i} - f_\mathrm{e}\right) \mathrm{d}v\right), \tag{8}$$

where $j \equiv e(Z\Gamma_\mathrm{i} - \Gamma_\mathrm{e})$ is the current density and $\Gamma_\alpha \equiv \int v f_\alpha \, \mathrm{d}v$ is the particle flux density. Two important assumptions are now made. It is assumed that, for all $x$ and $t$, the plasma is quasineutral,

$$n_\mathrm{e}\left(x,t\right) \approx Zn_\mathrm{i}\left(x,t\right), \tag{9}$$

and the rate of change of current density is negligible,

$$\left|\frac{1}{e}\frac{\partial j}{\partial t}\right| \ll \left|\frac{\partial}{\partial x}\int v^2 \left(Zf_\mathrm{i} - f_\mathrm{e}\right) \mathrm{d}v\right|. \tag{10}$$

In section 4.5, the validity of these two assumptions will be assessed via comparison with numerical solutions in which no such assumptions are made. Under assumptions (9) and (10), equation (8) becomes

$$e\frac{\partial \phi}{\partial x} = \frac{m_\mathrm{e} m_\mathrm{i}}{n_\mathrm{e}(Zm_\mathrm{e} + m_\mathrm{i})}\frac{\partial}{\partial x}\int v^2 \left(Zf_\mathrm{i} - f_\mathrm{e}\right) \mathrm{d}v. \tag{11}$$

Equations (1) and (11) are then a complete set which, for the initial conditions stated in section 3.1, can be solved analytically. Neglecting terms with a factor $m_e/m_i$, the distribution functions are given by Dorozhkina and Semenov (1998), Kovalev *et al* (2002)

$$f_\alpha = \frac{n_\alpha(x,t)}{(2\pi T_\alpha(t)/m_\alpha)^{1/2}} \exp\left(-\frac{(v-u)^2}{2T_\alpha(t)/m_\alpha}\right), \tag{12}$$

where

$$u(x,t) = u_\alpha \equiv \frac{1}{n_\alpha}\int v f_\alpha \,\mathrm{d}v = \frac{xt/\tau_\sigma^2}{1+(t/\tau_\sigma)^2} \tag{13}$$

is the ambipolar fluid velocity, $\tau_\sigma \equiv \sigma_0/c_s$ is the characteristic expansion time, and

$$c_s = \sqrt{\frac{T_{i0}+ZT_{e0}}{m_i+Zm_e}} \tag{14}$$

is the sound speed at the initial temperatures. Equation (12) states that both electron and ion distribution functions are Maxwellian *for all x and t*, with drift velocity $u$. Furthermore, the parallel temperature is constant in space and given by

$$T_\alpha(t) = \frac{T_{\alpha0}}{1+(t/\tau_\sigma)^2}, \tag{15}$$

and the density is

$$n_\alpha(x,t) = \frac{n_{\alpha0}}{\sqrt{1+(t/\tau_\sigma)^2}} \exp\left(\frac{e\phi(x,t)}{T_e(t)}\right). \tag{16}$$

Note that $n_e = Zn_i$ and the plasma is current-free, consistent with assumptions (9) and (10), respectively. The self-consistent potential has a quadratic dependence on $x$:

$$\phi(x,t) = \frac{-T_{e0}(x/\sigma_0)^2}{2e\left(1+(t/\tau_\sigma)^2\right)^2}, \tag{17}$$

i.e. the electric field is linear in $x$. This potential and its corresponding electric field, $E = -\partial\phi/\partial x$, will henceforth be referred to as the 'DS potential' and 'DS electric field', respectively, after the authors who first described it (Dorozhkina and Semenov 1998). Using (17) and defining $\sigma(t) \equiv \sigma_0\sqrt{1+(t/\tau_\sigma)^2}$, (16) can be written alternatively as

$$n_\alpha(x,t) = n_{\alpha0}\frac{\sigma_0}{\sigma(t)} \exp\left(-\frac{x^2}{2\sigma(t)^2}\right), \tag{18}$$

i.e. the density remains Gaussian at all times, with a monotonically increasing width $\sigma(t)$.

### 3.3. Flux densities

The most important quantities in terms of predictive ELM modelling are the particle and energy flux densities. For the Maxwellian distribution functions with drift velocity $u$ and temperature $T_\alpha$, these are given by

$$\Gamma_\alpha(x,t) \equiv \int v f_\alpha \,\mathrm{d}v = n_\alpha u, \tag{19}$$

$$Q_\alpha^x(x,t) \equiv \int \frac{1}{2}m_\alpha v^3 f_\alpha \,\mathrm{d}v = \Gamma_\alpha\left(\frac{1}{2}m_\alpha u^2 + \frac{3}{2}T_\alpha\right). \tag{20}$$

$Q_\alpha^x$ consists of a contribution $\frac{1}{2}m_\alpha u^2\Gamma_\alpha$ due to the kinetic energy of the parallel (directed) flow and another $\frac{3}{2}T_\alpha\Gamma_\alpha$ due to the convection of parallel (random) thermal energy. Note that *there is no heat flux density*:

$$q_\alpha^x(x,t) \equiv \int \frac{1}{2}m_\alpha(v-u)^3 f_\alpha \,\mathrm{d}v = 0, \tag{21}$$

since the velocity distributions are symmetric about $v = u$ (in this particular case they are Maxwellian). This means that, rather than solving the VP equations, the expansion could have been modelled equally well using a fluid closure which sets $q_\alpha^x = 0$. This has important consequences for the justification of using fluid models to model parallel ELM transport and will be discussed further in section 5.2.

For the *total* parallel energy flux density due to species $\alpha$, $Q_\alpha$, one must also account for the contribution $Q_\alpha^\perp$ due to the *parallel* convection of *perpendicular* (gyratory) thermal energy, i.e.

$$Q_\alpha(t) \equiv Q_\alpha^x + Q_\alpha^\perp. \tag{22}$$

As noted in section 2.3, this is accounted for in the 1D1V VP model by assuming a constant perpendicular temperature for both species equal to their initial parallel temperature. Each of the two perpendicular degrees of freedom in the drift plane then contributes $\frac{1}{2}\Gamma_\alpha T_{\alpha0}$ to $Q_\alpha^\perp$, so that in total

$$Q_\alpha^\perp(t) = \Gamma_\alpha T_{\alpha0}. \tag{23}$$

Unlike the parallel temperature, the perpendicular temperature is time independent. Thus, on timescales $t \gg \tau_\sigma$, the convected perpendicular thermal energy $\Gamma_\alpha T_{\alpha0}$ dominates over the convected parallel thermal energy $\frac{3}{2}\Gamma_\alpha T_\alpha$ since $T_\alpha \ll T_{\alpha0}$ (recall (15) for $t \gg \tau_\sigma$). For electrons, this means that $Q_e(t \gg \tau_\sigma) \approx Q_e^\perp$ while for ions $Q_i(t \gg \tau_\sigma) \approx Q_i^\perp + \frac{1}{2}m_i u^2\Gamma_i$.

### 3.4. Electron-to-ion energy transfer in the first few $\tau_\sigma$

It is worth emphasizing that the DS electric field remains linear at all times. It does not peak at the edge of the plasma bunch, where one would expect quasineutrality to break down, simply because quasineutrality is assumed *not* to break down. The field acts to confine the electrons (which oscillate back and forth inside the potential well) and to transfer kinetic energy from the electrons to the ions. To see this energy transfer, consider the total parallel stress,

$$P_\alpha(x,t) \equiv \int m_\alpha v^2 f_\alpha \,\mathrm{d}v = p_\alpha + n_\alpha m_\alpha u^2, \tag{24}$$

where $p_\alpha \equiv n_\alpha T_\alpha$ is the thermal pressure. The kinetic energy (per unit area in the drift plane) due to parallel motion is then

$$E_\alpha(t) \equiv \int \frac{1}{2}P_\alpha \,\mathrm{d}x = \frac{E_{\alpha0}}{1+(t/\tau_\sigma)^2}\left(1+\left(\frac{c_s}{v_{T\alpha}}\frac{t}{\tau_\sigma}\right)^2\right)$$
$$= E_\alpha^{\mathrm{th}}(t) + E_\alpha^{\mathrm{dy}}(t), \tag{25}$$

where $E_\alpha^{\mathrm{th}}$ is the thermal energy due to the random motion and $E_\alpha^{\mathrm{dy}}$ is the 'dynamic' energy due to the directed flow. Note that,

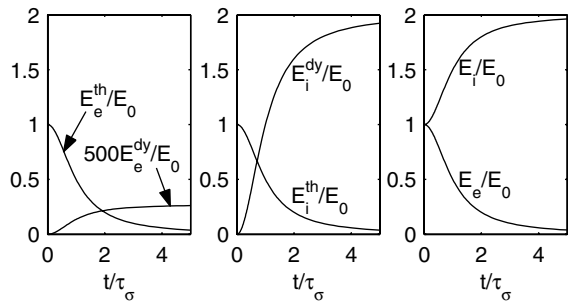


**Figure 1.** Thermal, dynamic and total energies for electrons and ions as a function of time for a hydrogen plasma with $T_{e0} = T_{i0}$, according to equation (25).

for this instantaneous-source expansion into an infinite space, the *total* kinetic energy remains constant at all times, i.e. the expansion is adiabatic:

$$E_i(t) + E_e(t) = E_{i0} + E_{e0} \qquad \forall t. \tag{26}$$

Also, since $n_e = Zn_i$, there is no contribution from the potential energy; $E_\phi \equiv \frac{e}{2}\int (Zn_i - n_e)\phi \, dx = 0$.

The thermal, dynamic and total energies for ions and electrons are plotted in figure 1 for a hydrogen plasma ($Z = 1$, $m_i/m_e = 1836$) with $T_{e0} = T_{i0}$ and $E_{e0} = E_{i0} = E_0$. Throughout the expansion, $E_e^{th} = E_i^{th}$ (in general, $E_e^{th} = (ZT_{e0}/T_{i0})E_i^{th}$). Initially, all of the energy is thermal. Then, due to the decreasing temperature, $E_\alpha^{th}$ decreases asymptotically to zero on a timescale $\tau_\sigma$. At the same time, the electric field accelerates the ions so that $E_i^{dy}$ increases from zero to $2E_0$ (in general $E_i^{dy}$ increases to $(c_s/v_{Ti})^2 E_{i0}$). Since the ion and electron fluid velocities are equal, $E_e^{dy}$ also increases, but by a negligible amount compared with $E_i^{dy}$ (in general $E_e^{dy}$ increases from zero to just $(c_s/v_{Te})^2 E_{e0} \approx 0$ due to the small electron mass). Thus, on a timescale $\tau_\sigma$, the energy allocation changes from being entirely thermal and equally shared between electrons and ions, to almost entirely dynamic and predominantly contained in the ions.

### 3.5. The free-streaming model in context

*3.5.1. Transition to the free-streaming phase.* For times $t \gg \tau_\sigma$ for the ions and $t \gg \sqrt{m_i/m_e}\tau_\sigma$ for the electrons, the DS electric field becomes too small to have any influence on the particle distribution functions (the longer timescale for the electrons is due to the electrons being more influenced by the electric field due to their lower mass; before $t \approx \sqrt{m_i/m_e}\tau_\sigma$, the electron thermal velocity is sufficient that electrons continue to be confined by DS potential well, oscillating inside it). Once the DS electric field becomes negligible for species $\alpha$, the distribution functions evolve according to the *force-free* Vlasov equation:

$$\frac{\partial f_\alpha}{\partial t} + v\frac{\partial f_\alpha}{\partial x} = 0, \tag{27}$$

which describes an advection of $f_\alpha$ along $x$ at velocity $v$ and has solution

$$f_\alpha(x, v, t) = f_\alpha(x - vt, v, t). \tag{28}$$

At this point, the particles can be said to 'free-stream' along $x$ under their inertia only.

*3.5.2. The free-streaming model is equation (12) for $\sigma_0 \to 0$.* In the limit $\sigma_0 \to 0$, the ions and electrons are all initially at the same point in space with initial density profile $n_\alpha(x, t = 0) = \sqrt{2\pi} n_{\alpha 0}\sigma_0 \delta(x)$. The electron–ion energy transfer, described in section 3.4, occurs instantaneously and the DS electric field decays in negligible time. Equation (12) gives the following solution:

$$f_\alpha^{FS} = \frac{n_{\alpha 0}\sigma_0}{c_s}\delta(x - vt)\exp\left(-\frac{v^2}{2c_s}\right), \tag{29}$$

where the 'FS' superscript signifies that the electrons and ions enter their free-streaming phases immediately.

Importantly, (29) is identical to the solution obtained if the potential is ignored and if the initial temperatures for the electrons and ions mimic their values after the energy transfer, i.e. if $\phi \to 0$ and $v_{T\alpha} \to c_s$. This can be seen by the fact that, in this hypothetical situation, the initial distribution function is

$$f_\alpha(t = 0) = \frac{n_{\alpha 0}\sigma_0}{c_s}\delta(x)\exp\left(-\frac{v^2}{2c_s}\right) \tag{30}$$

and the solution given by (28) is identical to (29). Thus, for $\sigma_0 \to 0$, the ions and electrons behave *as if* they originated from Maxwellian distributions with thermal speeds equal to $c_s$ (rather than $v_{T\alpha}$) and *as if* there were no electric field acting on them in their subsequent free-streaming along $x$.

This is a significant observation, since it lends credence to the free-streaming model (Fundamenski *et al* 2006), which is currently the primary analytic model for parallel transport in an ELM filament. The free-streaming model assumes that $\sigma_0 \to 0$ and that the Coulomb force can be ignored. In fact, the Coulomb force cannot be ignored. However, as was recognized above, in the $\sigma_0 \to 0$ case the acceleration of the ions is instantaneous so that a simple substitution $v_{Ti} \to c_s$ is sufficient to account for the Coulomb force. The free-streaming assumption is then simply that $\sigma_0 \to 0$.

In fact, the substitution $v_{Ti} \to c_s$ was made previously by Eich *et al* (2009). However, its rigorous justification via an analytic solution to the VP model is made here for the first time. In the next section, the particle and energy flux densities predicted by the free-streaming case ($\sigma_0 \to 0$) and by the more general case ($\sigma_0 \geqslant 0$) are compared. For both the particle and energy flux densities, the free-streaming assumption is seen to be appropriate wherever $x/\sigma_0 \gtrsim 5$.

*3.5.3. The free-streaming equations for flux densities.* The first velocity moment of (29) gives the particle flux density for the $\sigma_0 \to 0$ case:

$$\Gamma_\alpha^{FS}(x, t) = n_{\alpha 0}c_s\frac{x/\sigma_0}{(t/\tau_\sigma)^2}\exp\left(-\frac{(x/\sigma_0)^2}{2(t/\tau_\sigma)^2}\right). \tag{31}$$

Compare this with the general $\sigma_0 \geqslant 0$ case, obtained by substituting (13) and (18) into (19):

$$\Gamma_\alpha(x, t) = n_{\alpha 0}c_s\frac{(x/\sigma_0)(t/\tau_\sigma)}{\left(1 + (t/\tau_\sigma)^2\right)^{3/2}}\exp\left(-\frac{(x/\sigma_0)^2}{2\left(1 + (t/\tau_\sigma)^2\right)}\right). \tag{32}$$

Equation (31) is identical to that given previously by Fundamenski *et al* (2006) and Manfredi *et al* (2011) once the substitution $v_{T\mathrm{i}} \to c_\mathrm{s}$ is made.

Clearly, for $t \gg \tau_\sigma$ the free-streaming equation (31) is a good approximation to the $\sigma_0 \geqslant 0$ equation (32). There is a disagreement when $t \lesssim \tau_\sigma$ because, in the $\sigma_0 \geqslant 0$ case, the ions (which also determine the electron particle flux) have not yet entered their free-streaming phase. However, in a particular region, this disagreement can be ignored as long as the particle flux density in that region peaks long after $t = \tau_\sigma$. In fact, $\Gamma_\alpha^{\mathrm{FS}}$ peaks when

$$t = t_\Gamma^{\max}(x) = \frac{x/c_\mathrm{s}}{\sqrt{2}}. \tag{33}$$

Thus, (31) is a good approximation of (32) when $t_\Gamma^{\max} \gg \tau_\sigma$ in the region under consideration, i.e. where $x \gg \sigma_0$.

The same exercise can be carried out for the energy flux densities. Taking the third velocity moment of (29) and accounting for the convection of perpendicular energy (which contributes an additional $\Gamma_\alpha^{\mathrm{FS}} T_{\alpha 0}$), the parallel energy flux density for the $\sigma_0 \to 0$ case is

$$Q_\alpha^{\mathrm{FS}}(x,t) = \Gamma_\alpha^{\mathrm{FS}} T_{\alpha 0} \left\{ \frac{(x/\sigma_0)^2 (c_\mathrm{s}/v_{T\alpha})^2}{2(t/\tau_\sigma)^2} + 1 \right\}. \tag{34}$$

Compare this with the general $\sigma_0 \geqslant 0$ case, obtained by substituting (13) and (15) into (20), then (20) and (23) into (22):

$$Q_\alpha(x,t) = \Gamma_\alpha T_{\alpha 0} \times \left\{ \frac{(x/\sigma_0)^2 (t/\tau_\sigma)^2 (c_\mathrm{s}/v_{T\alpha})^2}{2\left(1 + (t/\tau_\sigma)^2\right)^2} + \frac{3/2}{1 + (t/\tau_\sigma)^2} + 1 \right\}. \tag{35}$$

For the ions, equation (34) is identical to that given previously by Fundamenski *et al* (2006) and Manfredi *et al* (2011) once the substitution $v_{T\mathrm{i}} \to c_\mathrm{s}$ is made. For the electrons, (34) is a new addition to the free-streaming equations. It says that electrons contribute to the parallel energy flux density almost entirely through the convection of their perpendicular thermal energy. This is because they donate almost all of their parallel energy to the ions instantaneously. Note that, unlike the $\sigma_0 \geqslant 0$ case, $Q_\alpha^{\mathrm{FS}}$ has no component due to the convection of parallel thermal energy (the second term in (35)), since the temperature at all positions goes immediately to zero (recall equation (15) for $\sigma_0 \to 0$).

Equation (34) is a good approximation to (35) when $t \gg \tau_\sigma$. At earlier times, the agreement breaks down because the ions have not yet entered their free-streaming phase. Note that, although the electrons do not enter their free-streaming phase until $t \sim \sqrt{m_\mathrm{i}/m_\mathrm{e}}\tau_\sigma$, $Q_\mathrm{e}^{\mathrm{FS}}$ still agrees with $Q_\mathrm{e}$ by the much earlier time $t \sim \tau_\sigma$. This is because, after $t \sim \tau_\sigma$, the energy transfer from electrons to ions means that $Q_\mathrm{e}$ is dominated by the convection of perpendicular energy, which is set by the ion particle flux. It is therefore of little consequence that equation (34) gets the component of the energy flux density due to *parallel* electron motion significantly wrong.

Applying the same argument as for the particle flux density, the total energy flux density in a particular region, $Q_\mathrm{tot} \equiv Q_\mathrm{e} + Q_\mathrm{i}$, will agree with the free-streaming value as long as it peaks long after $t = \tau_\sigma$. From (34), the *total* free-streaming energy flux density, $Q_\mathrm{tot}^{\mathrm{FS}} \equiv Q_\mathrm{i}^{\mathrm{FS}} + Q_\mathrm{e}^{\mathrm{FS}}$, peaks when

$$t = t_Q^{\max}(x) = 0.556 x/c_\mathrm{s}, \tag{36}$$

i.e. $t_Q^{\max}$ depends on the plasma parameters *only* through $c_\mathrm{s}$. Thus, for $Q_\mathrm{tot}^{\mathrm{FS}}$ to be a good approximation of $Q_\mathrm{tot}$, it is required that $t_Q^{\max} \gg \tau_\sigma$, i.e. that $x \gg \sigma_0$ in a given region.

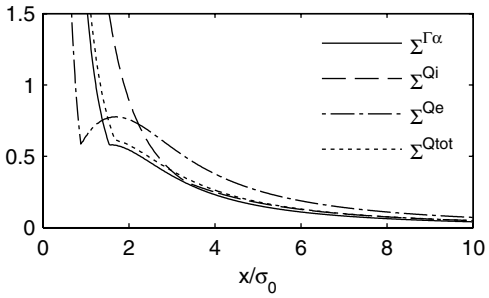


**Figure 2.** Level of agreement between free-streaming and $\sigma_0 \geqslant 0$ cases (measured by the function $\Sigma^\eta$) as a function of $x/\sigma_0$. Values for the particle, electron energy, ion energy and total energy flux densities are shown.

*3.5.4. The free-streaming equations are appropriate where $x/\sigma_0 \gtrsim 5$.* Instead of the rather vague statement that the free-streaming equations are a good approximation to the $\sigma_0 \geqslant 0$ case wherever $x \gg \sigma_0$, for practical purposes it is useful to quantify the level of approximation. To do this, the function $\Sigma^\eta$ is introduced:

$$\Sigma^\eta \equiv \frac{\max\left(\left|\eta - \eta^{\mathrm{FS}}\right|\right)}{\max\left(\eta\right)}, \tag{37}$$

where $\eta \in (\Gamma_\alpha, Q_\mathrm{i}, Q_\mathrm{e}, Q_\mathrm{tot})$ is some flux density and the maximum in (37) is taken over all time. Figure 2 shows $\Sigma^{\Gamma_\alpha}$, $\Sigma^{Q_\mathrm{i}}$, $\Sigma^{Q_\mathrm{e}}$ and $\Sigma^{Q_\mathrm{tot}}$ as a function of $x/\sigma_0$. An acceptable level of agreement ($\Sigma^\eta < 0.15$) is found for $\Gamma_\alpha$ and $Q_\mathrm{tot}$ in regions where $x/\sigma_0 > 5$. Note that $Q_\mathrm{e}$ requires slightly larger values of $x/\sigma_0$ before an acceptable agreement is found, because the electrons are not yet in their free-streaming phase.

It is concluded from this section that the free-streaming model for ELM parallel transport is in fact the same as the solution derived by Dorozhkina and Semenov (1998), for the particular case in which $\sigma \to 0$. Furthermore, in terms of the particle and energy flux densities it predicts, this assumption is reasonable wherever $x/\sigma_0 \gtrsim 5$.

### *3.6. On the assumption of an unbounded expansion*

The solution described by equations (12)–(17) assumes that the $x$-axis is unbounded. In the case of a bounded plasma, with the boundary condition $f_\alpha(x = \pm L, v, t) = \phi(x = \pm L, t) = 0$, it is expected that a sheath potential $\phi_\mathrm{s}$ will be set up at the target, over a width approximately equal to the local Debye length. If $L/\sigma_0 \gg 1$, however, the majority of electrons, which will reach the target at the same time as the ions on a timescale $\tau_L \equiv L/c_\mathrm{s}$, will have lost the majority of their energy to the ions by the time they reach the target, and will not have

sufficient energy to set up a significant sheath potential. This can be seen quantitatively by estimating the sheath potential $\phi_s$ created by inserting a boundary at $x = L$, under the assumption that the ion and electron dynamics away from the sheath are unaffected by its presence. The goal is then to find the value of $L/\sigma_0$ which is sufficiently small that the calculated value of $\phi_s$ *would*, in fact, alter the dynamics away from the sheath.

A similar approach by Stangeby (2000) is used to estimate $\phi_s$. In the absence of a particle source inside the sheath, the ion flux density to the wall, $\Gamma_i^w(t)$, is unchanged relative to its value at the sheath edge. Assuming that the thickness of the sheath is negligible, this gives

$$\Gamma_i^w(t) = n_i(x = L, t)u(x = L, t), \tag{38}$$

where $u$ and $n_i$ are given by (13) and (16). It is also assumed that the electron density is given by a Boltzmann relation in the sheath, and that the electron distribution function at the wall is a half-Maxwellian with zero drift velocity and with no backward-moving electrons. Such a distribution, with density $n_e^H$ ('H' for 'half') and local thermal velocity $v_{Te}^H$ has particle flux density $\sqrt{2/\pi}n_e^H v_{Te}^H$. The electron flux density to the wall is therefore

$$\Gamma_e^w(t) = \sqrt{\frac{2}{\pi}}n_e(x = L, t) \times \exp\left(\frac{e\phi_s}{T_e(x = L, t)}\right)\sqrt{\frac{T_e(x = L, t)}{m_e}}. \tag{39}$$

Assuming zero current density into the target, $Z\Gamma_i^w(t) + \Gamma_e^w(t) = 0$, yields

$$\frac{e\phi_s}{T_{e0}} = \frac{1}{1 + (L/\sigma_0)^2(t/\tau_L)^2} \times \ln\left(Z^2\sqrt{\frac{\pi}{2}}(c_s/v_{Te})\frac{(L/\sigma_0)^2(t/\tau_L)}{\sqrt{1 + (L/\sigma_0)^2(t/\tau_L)^2}}\right) \tag{40}$$

for the sheath potential as a function of time.

It is assumed that the dynamics of the plasma expansion will be significantly altered by the presence of a target sheath when the work done on the plasma by the sheath, $U_s$, is of a similar order to the work done by the DS potential, $U_{DS}$. By energy conservation, $U_{DS}$ in the region $-L \leqslant x \leqslant L$ is the total increase in ion kinetic energy in the infinite region minus the energy made unavailable by electron energy transport through $x = -L$ and $x = L$:

$$U_{DS}(t) = (E_i(t) - E_{i0}) - 2\int_0^t Q_e^x(x = L, t')\,dt', \tag{41}$$

while $U_s$ is equal to the time integral of the sheath potential multiplied by the electron flux through $x = -L$ and $x = L$:

$$U_s(t) = -2e\int_0^t \phi_s(t')\Gamma_e^x(x = L, t')\,dt'. \tag{42}$$

Figure 3 compares $U_{DS}$ and $U_s$ (normalized to $E_{e0}$), as functions of $t/\tau_L$ for different values of $L/\sigma_0$. It is seen that for $L/\sigma_0 \gtrsim 5$ the work done by the DS potential is dominant. For $L/\sigma_0 = 2$, however, the work done by the sheath is dominant. It is therefore expected that the sheath will have a

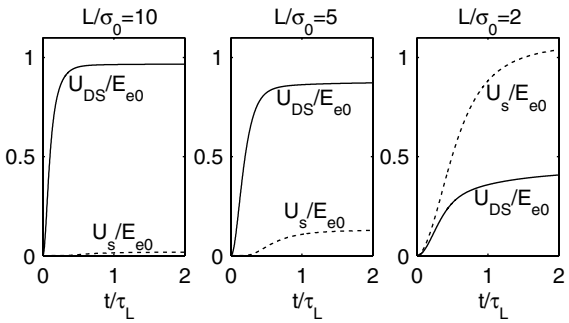


**Figure 3.** Work done by the DS potential in the bounded region $-L \leqslant x \leqslant L$ compared with the work done by the sheath potential predicted by equation (40), for different values of $L/\sigma_0$.

significant effect on the plasma dynamics for values $L/\sigma_0 \lesssim 5$. It is important to note that this is the same condition that was required for the free-streaming target flux densities to be valid. Thus, for the target flux densities, if the sheath can be ignored then so can the fact that the filament has a finite parallel extent.

### *3.7. On the assumption of quasineutrality*

A quasineutral region is defined where $|x| \lesssim \sigma_q(t)$. The quasineutral assumption requires that this region extends over several plasma widths at all times:

$$\sigma_q(t)/\sigma(t) > O(1) \qquad \forall t. \tag{43}$$

At the points $x = \pm\sigma_q$, where the plasma ceases to be quasineutral, it is assumed that the local gradient length in the electron density is approximately equal to the local Debye length:

$$\left.\frac{n_e}{|\partial n_e/\partial x|}\right|_{x=\sigma_q} \approx \lambda_D, \tag{44}$$

where $\lambda_D(x, t) = \sqrt{\varepsilon_0 T_e/e^2 n_e}$. Assuming that the quasineutral solutions are valid in the quasineutral region, (15) and (16) can be substituted into (44) and the resulting equation can be solved for $\sigma_q$, giving

$$\frac{\sigma_q(t)}{\sigma(t)} \approx \sqrt{2W\left(\frac{\left(1 + (t/\tau_\sigma)^2\right)^{3/2}}{2(\lambda_{D0}/\sigma_0)^2}\right)}, \tag{45}$$

where $\lambda_{D0} \equiv \lambda_D(x = 0, t = 0)$ and $W(a)$ is the Lambert $W$ function, which is the solution to $xe^x = a$ (Valluri *et al* 2000). Equation (45) is plotted in figure 4, for different values of $\lambda_{D0}/\sigma_0$.

It is seen that, as $\lambda_{D0}/\sigma_0$ decreases, the quasineutral region extends over an increasing portion of the expanding plasma. Furthermore, $\sigma_q/\sigma$ is a monotonically increasing function of time. This means that, as the plasma expands, the width of the initially quasineutral region can only get wider relative to the width of the expanding plasma:

$$\frac{\sigma_q(t > 0)}{\sigma(t > 0)} > \frac{\sigma_q(t = 0)}{\sigma_0} \qquad \forall t. \tag{46}$$

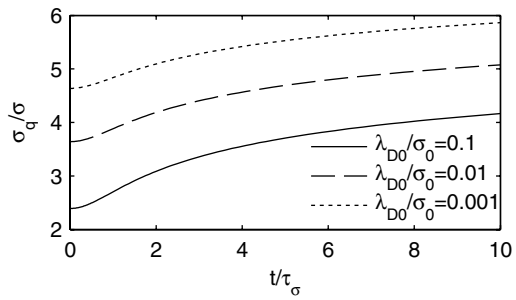


**Figure 4.** Plot of the width of the quasineutral region compared with the width of the expanding plasma, according to equation (45), for different values of $\lambda_{D0}/\sigma_0$.

Inserting (45) into (43), the quasineutrality requirement therefore reduces to a requirement on the initial conditions only:

$$\sqrt{2W\left(\frac{1}{2(\lambda_{D0}/\sigma_0)^2}\right)} > O(1). \tag{47}$$

Thus, *if the quasineutrality condition holds initially in the bulk of the plasma then it will hold at all times*. Note that this hypothesis was also previously made by Manfredi *et al* (1993) and Dorozhkina and Semenov (1998). However, an equation for the width of the quasineutral region, such as (45), was not derived. Furthermore, in this work (45) will be verified by comparison with a numerical solution to the VP model in which quasineutrality was *not* assumed (see section 4.5).

## 4. Numerical results

In this section, numerical solutions to the VP model are presented. For the instantaneous-source case, these solutions allow for a comparison between the analytic solution and its numerically solved counterpart. The validity of the various assumptions made in deriving the analytic solution are assessed by means of numerical simulations in which those assumptions are not made. In particular, the assumptions of quasineutrality, of a slowly varying current density, of an unbounded parallel coordinate, of a $1v$ collisionless plasma, and of a Gaussian initial density, will be assessed. The effect of a finite source duration (for which an analytic solution is unavailable) will also be investigated.

### *4.1. Dimensionless input parameters and the 'reference' simulation*

The minimum set of dimensionless input parameters for the bounded VP model is as follows (values in brackets are those that were used for the 'reference' simulation):

- $m^* \equiv m_i/m_e$ $(= 1836)$, the mass ratio,
- $Z$ $(= 1)$, the proton number,
- $T^* \equiv T_{i0}/T_{e0}$ $(= 1)$, the temperature ratio of the injected particles,
- $\lambda^*_{D0} \equiv \lambda_{D0}/\sigma_0$ $(= 10^{-2})$, the normalized Debye length,
- $L^* \equiv L/\sigma_0$ $(= 10)$, the normalized connection length,
- $\tau^*_{src} \equiv \tau_{src}/\tau_\sigma$ $(= 0)$, the normalized source duration.

### *4.2. Solution methods*

Unless otherwise stated, the numerical solutions presented here were calculated by the code previously described by Manfredi *et al* (2011). Henceforth, this code will be called VESPA (Vlasov Eulerian Simulator of PArallel transport). For a detailed description of the VESPA code, the reader is referred to Manfredi *et al* (2011). For this paper, the two important points to note are the following:

(a) Numerical stability was ensured by always using a grid spacing of $\Delta x = \lambda_{D0}$ along $x$ and a time step $\Delta t = 1/\omega_{pe0}$, where $\omega_{pe0} \equiv v_{Te}/\lambda_{D0}$ is the electron plasma frequency at electron density $n_{e0}$ and electron temperature $T_{e0}$.

(b) The actual value used for $\lambda^*_{D0}$ was typically $10^{-2}$, which is significantly higher than the ELM-realistic value of $\lambda^*_{D0} \lesssim 10^{-5}$ (see section 5.1.4).

This last point requires some explanation, since it is essential if the code is to run on an acceptable timescale (using $\lambda^*_{D0} = 10^{-2}$, the solution time on a modern desktop is ∼30 h, but this time quickly increases for smaller values of $\lambda^*_{D0}$, scaling roughly with $\lambda^{*-2}_{D0}$). It was already recognized by Manfredi *et al* (2011) that the difference in the numerical solution when $\lambda^*_{D0} = 10^{-2}$ and when $\lambda^*_{D0} = 2.5 \times 10^{-3}$ is negligible. In fact, this is precisely because the assumption of quasineutrality is valid in the bulk plasma whenever $\lambda^*_{D0} \lesssim 10^{-2}$. The solution for the bulk plasma is therefore independent of $\lambda^*_{D0}$ for $\lambda^*_{D0} \lesssim 10^{-2}$. This will be discussed further in sections 4.5 and 4.7.

In addition to the VESPA code, the 1D3V particle-in-cell code BIT1 was also used to solve the VP model. For details of this code the reader is referred to Tskhakaya and Schneider (2007), Tskhakaya *et al* (2008). The important points to note for this article are that:

(i) The particle-in-cell method employed by BIT1 allows it to be massively parallelized. This means that *realistic* values for $\lambda^*_{D0}$ can be modelled, by spreading the computational load over several thousand processors. The hypothesis that the solution with $\lambda^*_{D0} = 10^{-2}$ is negligibly different to the solution with a realistic value of $\lambda^*_{D0}$ can therefore be directly tested.

(ii) BIT1 is able to include collisions. It is also three-dimensional in velocity space, so that parallel and perpendicular distribution functions can affect each other, via collisions. The assumption of a $1v$ collisionless plasma can therefore be assessed.

### *4.3. Reference simulation matches analytic solution inside the quasineutral region*

*4.3.1. Comparison for the densities and electric field.* Figure 5(*a*) shows the reference simulation values for $n_e$ (solid red lines) and $n_i$ (solid blue lines) at $t = 0.01\tau_\sigma$, $t = \tau_\sigma$ and $t = 10\tau_\sigma$. These times span the entire expansion process, from the initial setup of the electric field in the quasineutral region, until after the particle flux density to the target has peaked (when $t = 7.1\tau_\sigma$). The significance of $t = 0.01\tau_\sigma$

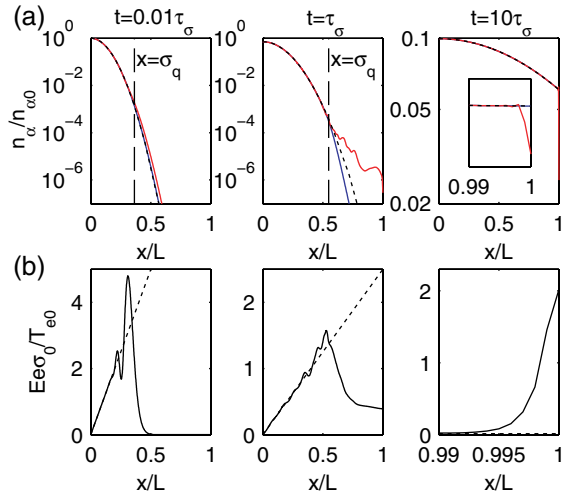


**Figure 5.** (*a*) Comparison between $n_e$ (solid red lines) and $n_i$ (solid blue lines) for the reference simulation and for the analytic solution predicted by (16) (dotted black lines). Plots are made at $t = 0.01\tau_\sigma$, $t = \tau_\sigma$ and $t = 10\tau_\sigma$. The $x = \sigma_q$ lines predicted by (45) are plotted as dashed black lines. The inset axis in the final panel is zoomed into the sheath region and has the same $y$-axis limits as the main panel. (*b*) Comparison between the electric field for the reference simulation (solid lines) and for the analytic solution predicted by (17) (dotted lines), at the same times as plotted in (*a*).

is explained below. Plots are shown only in the positive-$x$ region since the solution is symmetric about $x = 0$. The simulation values should be compared with the black dotted lines, which plot equation (16) for the analytic prediction of the density evolution. Also plotted, as black dashed lines at times $t = 0.01\tau_\sigma$ and $t = \tau_\sigma$, are the lines $x = \sigma_q$, which correspond to the edges of the quasineutral region predicted by equation (45). These predictions are seen to coincide well with the position at which quasineutrality breaks down in the simulation (see section 4.5 for a more thorough verification of (45)). Note that at all times the vast majority (>99.9%) of the plasma is contained within this quasineutral region. For the $t = 10\tau_\sigma$ panel, $\sigma_q$ is not plotted since by that time the edge of the quasineutral region is at the entrance to the target sheath rather than at the edge of the expanding plasma.

Inside the quasineutral region, the reference simulation values for $n_e$ and $n_i$ agree well with equation (16). This is true at all times. Outside the quasineutral region and before the bulk plasma reaches the boundary (as shown in the $t = 0.01\tau_\sigma$ and $t = \tau_\sigma$ panels), $n_e$ is greater than the analytic prediction due to suprathermal electrons escaping the confining electric field. In contrast, $n_i$ is lower than the analytic prediction because the electric field is weaker than predicted by equation (17). In fact, the suprathermal electrons leave the quasineutral region in bunches, rather than as a constant stream. This causes a wavelike density profile outside the quasineutral region, as seen in the $t = \tau_\sigma$ panel of figure 5(*a*). This behaviour, although physically interesting, does not appear to affect the solution inside the quasineutral region, nor is it important in terms of energy flux densities to the target. It will not, therefore, be analysed further in this paper.

Once the bulk plasma reaches the boundary, which it has done by time $t = 10\tau_\sigma$, the edge of the quasineutral region becomes defined by the sheath. Inside the sheath, $n_e < n_i$, as can be seen in the zoomed-in version of the $t = 10\tau_\sigma$ panel, inset. Importantly, however, at no point in time does the presence of a sheath at the boundary has a significant effect on the excellent level of agreement with the analytic density evolution inside the quasineutral region.

Figure 5(*b*) plots the electric field corresponding to the densities shown in figure 5(*a*). Reference simulation and analytic values are plotted as solid and dotted lines, respectively. From an initial plasma that is perfectly neutral, electron motion sets up a local electric field on a timescale given by the inverse of the *local* electron plasma frequency, $\omega_{pe}(x, t)$. Since $\omega_{pe} \propto \omega_{pe0}\sqrt{n_e}$, the linear electric field takes time to spread out from $x = 0$ (where the plasma is most dense) to $x = \sigma_q$ (where the plasma is less dense). By time $t = 1/\omega_{pe}(x = \sigma_q, t = 0) = 0.01\tau_\sigma$, an electric field which agrees well with equation (17) is set up across the entire quasineutral region (this explains why plots have been made at $t = 0.01\tau_\sigma$).

Outside the quasineutral region and before the bulk plasma reaches the boundary, the electric field decays to zero, as it must since the charge density is finite. By the time the sheath is set up at the boundary, the electric field has decayed to ∼0 inside the quasineutral region and the sheath electric field (which extends over several $\lambda_{D0}$) is dominant. This is shown in the $t = 10\tau_\sigma$ panel (note the change in $x$-axis limits for this panel and that $\lambda_{D0} = 0.001L$ for this simulation). Importantly, however, this sheath electric field is too weak to alter the dynamics of the density expansion inside the quasineutral region.

*4.3.2. Comparison for the temperatures and fluid velocity.* Figure 6(*a*) shows $T_e$ (solid red lines) and $T_i$ (solid blue lines) in the reference simulation, at the same times as plotted in figure 5 ($T_\alpha$ is defined as $T_\alpha \equiv \int m_\alpha (v - u_\alpha)^2 f_\alpha \, dv/n_\alpha$). The analytic solution given by (15), which is constant in space and equal for ions and electrons, is plotted as black dotted lines. Again, the agreement in the quasineutral region is good. The decrease in $T_e$ outside the quasineutral region is due to the fact that the energy contained in the suprathermal electrons which escape the confining potential is primarily dynamic; the decrease does *not* imply that the escaping electrons are sub-thermal. By time $t = 10\tau_\sigma$, there is a small decrease in $T_e$ inside the quasineutral region, compared with (15). This is due to the formation of a boundary sheath, and the fact that only suprathermal electrons can overcome the sheath potential and reach the wall. The resultant effect on $T_e$ is small, however, reducing it by only 17% at the sheath edge, compared with the analytic solution.

Figure 6(*b*) compares $u_i$ in the reference simulation (solid lines) and as predicted by equation (13) (dotted lines). Note that $u_i$ is normalized to the *initial* sound speed; $u_i/c_s$ is *not* the local Mach number, which increases with decreasing temperature and is given by $M = (u_i/c_s)\sqrt{T_{i0}/T_i}$. At $t = 10\tau_\sigma$, for example, $u_i/c_s = 1$ at the target, while $M = 10.0$. As for $n_\alpha$, $E$ and $T_\alpha$, the reference simulation values for $u_i$ agree well with the analytic solution inside the quasineutral region at all times. Outside the quasineutral region, $u_i$ is lower than the analytic prediction because the

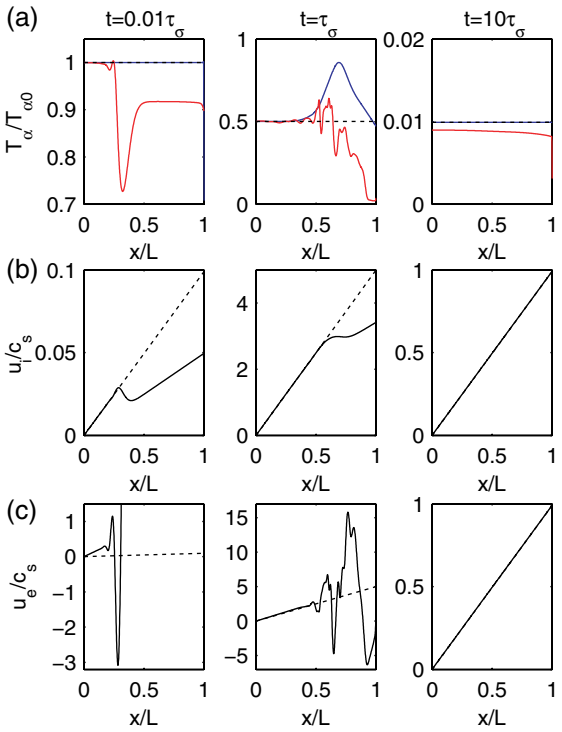


**Figure 6.** (*a*) Comparison between $T_e$ (solid red lines) and $T_i$ (solid blue lines) for the reference simulation and for the analytic solution predicted by (15) (dotted black lines). Plots are made at the same times as in figure 5. (*b*)–(*c*) Comparison between $u_i$ (*b*) and $u_e$ (*c*) for the reference simulation (solid lines) and for the analytic solution predicted by (17) (dotted lines), at the same times as plotted in (*a*).

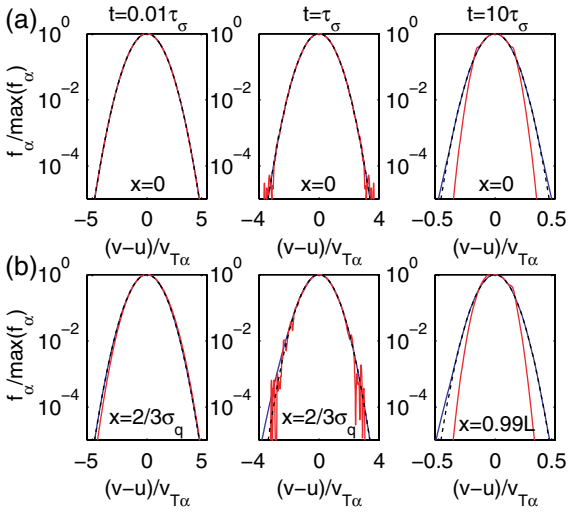


**Figure 7.** Comparison between $f_e$ (solid red lines) and $f_i$ (solid blue lines) for the reference simulation and for the analytic solution predicted by (12) (dotted black lines). Plots are made at the same times as in figures 5 and 6. In (*a*) plots are made at $x = 0$, while in (*b*) plots are made either at $x = 2/3\sigma_q$ or at $x = 0.99L$, as indicated.

accelerating electric field is also lower, as was shown in figure 5.

Figure 6(*c*) makes the same comparison for $u_e$ (recall that in the analytic solution $u_e = u_i$ at all times). At $t = 0.01\tau_\sigma$ in the quasineutral region, the simulated $u_e$ exceeds (13) by a constant factor 16.3. This is because, for the value of $\lambda^*_{D0}$ used in the simulation, the timescale on which electrons move across the plasma, $\sigma_0/v_{Te}$, is not significantly shorter than the timescale on which the electric field is set up across the quasineutral region: $0.01\tau_\sigma = 0.3\sigma_0/v_{Te}$. As a result, suprathermal electrons, which start off at the edge of the quasineutral region, and which have sufficiently positive velocities that they escape the potential well, are not reflected backwards in the negative-$x$ direction. They are therefore unable to provide a counter to the forward moving suprathermal electrons which start off deeper inside the bulk plasma. These remaining electrons contribute to a positive $u_e$ inside the quasineutral region that is significantly larger than in the analytic solution, in which *all* of the electrons are confined and oscillate in the potential well in precisely such a way that $u_e = u_i$. The important point is that the degree to which $u_e$ exceeds equation (13) in the quasineutral region at early times is dependent on the flux of electrons that are able to overcome the confining potential (and therefore do not oscillate back). This flux decreases with decreasing $\lambda^*_{D0}$ (Manfredi *et al* 2011), so that the agreement with (13) is expected to improve markedly for more realistic (lower) values than the value of $\lambda^*_{D0} = 10^{-2}$ used in the reference simulation. Indeed, in a simulation with $\lambda^*_{D0} = 10^{-3}\, u_e$ was found to exceed (13) in the quasineutral region by a constant factor of only 6.5. Realistic values of $\lambda^*_{D0} \lesssim 10^{-5}$ (see section 5.1.4) are therefore expected to eliminate the disagreement with (13).

At the edge of the quasineutral region, $u_e$ drops suddenly in the reference simulation, due to electrons being reflected back towards the bulk. It then rises monotonically to $\sim 80/c_s = 2.6v_{Te}$ at the target (this rise is not visible on the axes chosen for this plot). This is because, as previously stated, the energy in the escaping suprathermal electrons is predominantly dynamic.

By time $t \approx 0.1\tau_\sigma$, and at all subsequent times (the first shown being $t = \tau_\sigma$), $u_e$ does agree well with (13) in the quasineutral region and the plasma is ambipolar there. Outside the quasineutral region, $u_e$ is highly non-linear due to the oscillations of high-energy electron bunches, which are themselves dependent on the value of $\lambda^*_{D0}$ used. Fortunately, the behaviour in this region is not important when trying to predict the energy flux densities at the targets, which are dependent on the dynamics inside the quasineutral region, where the vast majority of the plasma is found.

*4.3.3. Comparison for the distribution functions.* Values of $f_e$ and $f_i$ for the reference simulation are plotted in figure 7, as red and blue solid lines, respectively, at the same times as plotted in figures 5 and 6. In figure 7(*a*) plots are made at $x = 0$, while in figure 7(*b*) plots are made towards the edge of the quasineutral region, at $x = 2/3\sigma_q$ (for the $t = 0.01\tau_\sigma$ and $t = \tau_\sigma$ panels) and at $x = 0.99L$ (i.e. at the sheath entrance, for the $t = 10\tau_\sigma$ panel). In all plots, distribution function values are normalized to their maxima and plotted as a function of $(v-u)/v_{T\alpha}$, where $u$ is calculated using (13). For comparison, the analytic solution from (12) is plotted as black dotted lines.

At all times, the simulated $f_i$ agrees well with the analytic Maxwellian solution (12) inside the quasineutral region. For the simulated $f_e$, however, there is some deviation from (12).

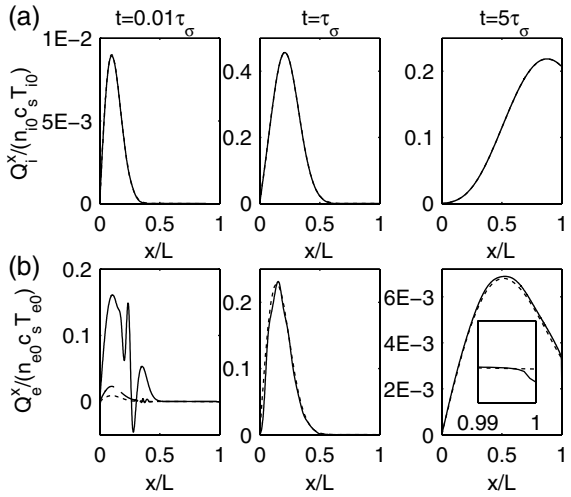


**Figure 8.** Comparison between (*a*) $Q_\mathrm{i}$ and (*b*) $Q_\mathrm{e}$ for the reference simulation (solid lines) and for the analytic solution predicted by (35) (dotted black lines). Plots are made at $t = 0.01\tau_\sigma$, $t = \tau_\sigma$ and $t = 5\tau_\sigma$. In the $t = 0.01\tau_\sigma$ panel of (*b*), the dashed line shows values an identical simulation to the reference simulation, but with $\lambda^*_{\mathrm{D}0} = 10^{-3}$. The inset axis in the final panel is zoomed into the sheath region and has the same $y$-axis limits as the main panel.

When $t = 0.01\tau_\sigma$, the deviation (which is due to the loss of suprathermal electrons as explained in the previous section) is not obvious, primarily because $u_\mathrm{e} \ll v_{T\mathrm{e}}$. However, as will be seen in figure 8, this deviation does cause a significant departure from the analytic electron energy flux density predicted by (35). When $t = \tau_\sigma$, especially towards the edge of the quasineutral region, there is a departure of $f_\mathrm{e}$ from (12). Again, this is due to the loss of suprathermal electrons from the confining potential and the agreement between analytic and simulated values for $f_\mathrm{e}$ is expected to improve for lower (more realistic) values of $\lambda^*_{\mathrm{D}0}$ than used in the reference simulation. Still, even for the (unphysically high) value of $\lambda^*_{\mathrm{D}0} = 10^{-2}$ used in the reference simulation, the electron distribution function approximates well to the analytic Maxwellian solution over several orders of magnitude. By time $t = 10\tau_\sigma$, $f_\mathrm{e}$ narrows slightly compared with the analytic solution (i.e. $T_\mathrm{e}$ decreases). This is due to the loss of suprathermal electrons which overcome the target sheath potential, as described in the previous section. Overall, however, the prediction that the distribution functions remain Maxwellian throughout is well met in the quasineutral region of the reference simulation.

*4.3.4. Comparison for the energy flux densities.* Figure 8 shows (*a*) $Q^x_\mathrm{i}$ and (*b*) $Q^x_\mathrm{e}$ in the reference simulation (solid lines) and according to (35) (dotted lines). Note that, since $Q_\mathrm{tot}$ peaks at the target when $t = 5.6\tau_\sigma$, the final panels in this figure show plots at $t = 5\tau_\sigma$ rather than at $t = 10\tau_\sigma$ as in the previous figures.

Simulated values for $Q^x_\mathrm{i}$ agree with (35) at all times (the dotted lines are obscured in figure 8 because they overlay the solid lines). By time $t = 5\tau_\sigma$, the majority of the energy flux density due to parallel motion is provided by the kinetic energy of the ion flow. For the electrons, there is a marked disagreement between simulated and analytic values when $t = 0.01\tau_\sigma$. This is caused primarily by the larger value of $u_\mathrm{e}$ compared with (13), but also by the asymmetry of $f_\mathrm{e}$ about $v = u_\mathrm{e}$, which generates a heat flux density. Importantly this disagreement is almost eliminated by a more realistic choice of $\lambda^*_{\mathrm{D}0} = 10^{-3}$, as shown by the dashed line in the $t = 0.01\tau_\sigma$ panel of figure 8(*b*). This disagreement is expected to be completely eliminated for realistic values of $\lambda^*_{\mathrm{D}0} \lesssim 10^{-5}$. By time $t = \tau_\sigma$, the simulated $Q^x_\mathrm{e}$ agrees well with (35). At time $t = 5\tau_\sigma$, the sheath acts to decrease $Q^x_\mathrm{e}$ at the boundary by 40% compared with (35). This can be seen in the zoomed-in plot, inset. However, this decrease has a negligible effect on the total electron energy flux to the target, which is due primarily to the convection of perpendicular thermal energy.

It is concluded from this section that the analytic solution agrees well with the reference simulation inside the quasineutral region and that the disagreement outside the quasineutral region does not affect the agreement inside.

### *4.4. The role of the target sheath*

*4.4.1. The sheath has negligible effect on target flux densities when $L^* \gtrsim 5$.* Of particular interest are the levels of agreement between analytic and numerical solutions for the particle and energy flux densities to the target which, as explained in section 3.6, are expected to get worse as $L^*$ decreases and the target sheath plays an increasingly important role. A scan in $L^*$ was therefore performed, comprising three simulations with values of $L^* = 10$ (the reference simulation), $L^* = 5$ and $L^* = 2$. Due to the ballooning nature of the ELM filament source, values lower than $L^* = 2$ are likely to be unphysical, so were not explored (see section 5.1.5 for further discussion).

Figure 9 plots $\Gamma_\mathrm{i}$, $Q^x_\mathrm{i}$, $Q^x_\mathrm{e}$ and $Q_\mathrm{tot}$ at the target, for the numerical simulations (solid lines) and analytic predictions (dotted lines) given by equations (32), (22) and (35). The different values of $L^*$ are denoted by different colours, as described in the legend. Note that only $\Gamma_\mathrm{i}$ is shown since, as expected, $\Gamma_\mathrm{e}$ is very well approximated by $\Gamma_\mathrm{i}$ in the simulations.

For the reference simulation (black solid lines) the differences between the analytic and numerical flux densities at the target are negligible. The sheath can therefore be ignored at this value of $L^*$. For values of $L^* \lesssim 5$ (as predicted in section 3.6) the sheath starts to become important in the simulations, at least in terms of energy exchange between electrons and ions. This is clearly seen for the $L^* = 2$ simulation, in which the sheath acts to increase $Q^x_\mathrm{i}$ and decrease $Q^x_\mathrm{e}$ at the target, compared with the analytic predictions of equation (35). However, even at this value of $L^*$ (which appears to be right at the lowest bound of what can be expected in experiment; see section 5.1.5), the agreement for the *total* energy flux density, figure 9(*d*), is still acceptable. That is, the sheath acts only to alter the partition of ion and electron energies reaching the target, but does not affect the dynamics of the plasma expansion to the target.

As a brief aside, it should be noted that there is a burst of suprathermal electrons in the simulations, which arrive at the target on a timescale $L/v_{T\mathrm{e}}$. Such electron bursts are also

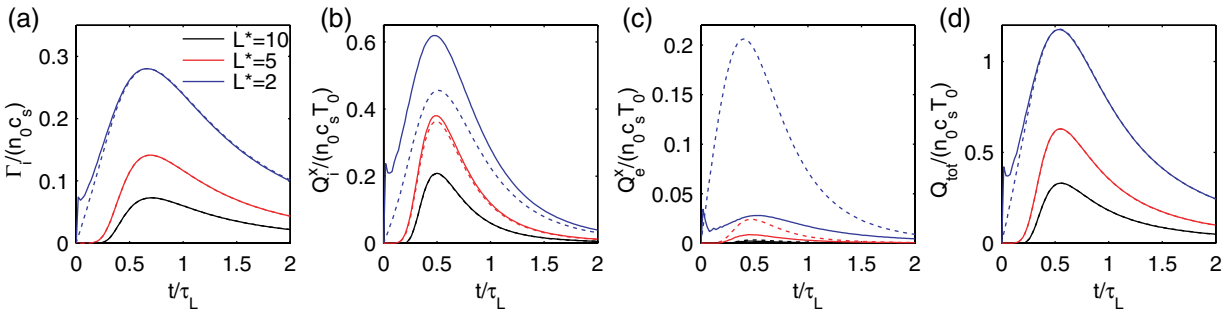


**Figure 9.** Comparison of (*a*) $\Gamma_i$, (*b*) $Q_i^x$, (*c*) $Q_e^x$ and (*d*) $Q_{tot}$ at the target, for the analytic solutions (dotted lines) and numerical VESPA solutions (solid lines), for $L^* \in \{10, 5, 2\}$, as labelled in (*a*).

observed in experiment (Loarte *et al* 2003) and have been analysed more thoroughly by Manfredi *et al* (2011). The resulting target flux densities, which are due to a breakdown in quasineutrality, are not captured by the analytic solution. However, compared with the flux densities delivered by the >99.9% of plasma inside the quasineutral region (which *is* captured by the analytic solution), the fluxes delivered by these suprathermal electrons is negligible, and inconsequential in terms of engineering concerns.

*4.4.2. Comparison between predicted and simulated sheath potentials.* In order to assess the accuracy of the sheath potential predicted by equation (40), the simulated sheath potential is defined as

$$\phi_s \equiv \phi_2(x = L) - \phi_1(x = L), \tag{48}$$

where $\phi_1$ and $\phi_2$ are the potentials in a simulation bounded at $x = \pm L$ and at $x = \pm 2L$, respectively (both $\phi_1$ and $\phi_2$ are renormalized so that $\phi_1(x = 0) = \phi_2(x = 0)$). Thus, for each simulation in the $L^*$ scan, the connection length was doubled whilst leaving all other parameters the same. For all three simulations, this had the desired effect of removing any sheath effects at $x = L$, at least for times after the quasineutral region reaches the boundary. This was confirmed by observing that the analytic (unbounded) solutions for $f_e$ and $f_i$ were recovered at $x = L$ when the connection length was doubled in the simulation (before the quasineutral region reaches the boundary, the analytic solution at $x = L$ is incorrect so it is not possible to be sure that the effect of a boundary has been removed).

Figure 10 shows the simulated sheath potential (solid lines) compared with the theoretical prediction of equation (40) (dotted lines) for different values of $L^*$, as a function of $t/\tau_L$. The time when the quasineutral region reaches the boundary, i.e. when $\sigma_q(t) = L$ according to equation (45), is indicated by dashed red lines (no line is shown for the $L^* = 2$ simulation since $\sigma_q(t = 0) > L$).

Before the quasineutral region reaches the boundary, there is a clear discrepancy between equation (40) and the simulation result in all three simulations. Assuming that doubling the connection length *did* remove the effect of the sheath at these early times, this discrepancy can be explained by the fact that, before the quasineutral region reaches the boundary, the sheath potential is set by suprathermal electrons. For

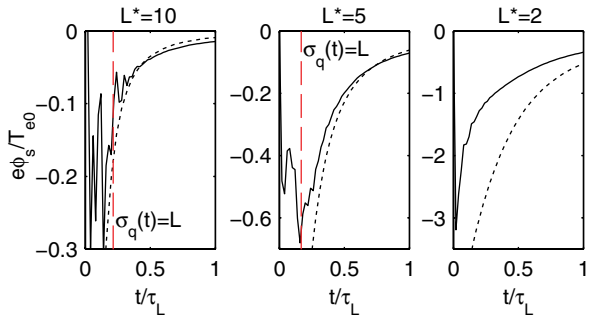


**Figure 10.** Comparison between the theoretical (dotted lines) and simulated (solid lines) sheath potential as a function of time, for different values of $L^*$. Theoretical values were calculated using equation (40). The time when the quasineutral region reaches the boundary (according to equation (45)) is indicated by red dashed lines.

these electrons, the assumption of a Boltzmann distributed density which was made in the derivation of (40) will be wrong. After the quasineutral region reaches the boundary, the agreement between (40) and the simulation result is quite reasonable, although the agreement worsens for smaller values of $L^*$. An explanation for this might be that, for small $L^*$, the sheath potential is sufficiently strong that $T_e$ at the sheath edge is significantly reduced relative to the unbounded solution. This would have the effect of reducing the magnitude of $\phi_s$ in the simulation compared with (40). Nevertheless, for experimentally realistic values of $L^*$, equation (40) provides a reasonable agreement with the numerical result after the quasineutral region reaches the boundary.

### *4.5. Verification of quasineutral and current density assumptions*

It has been demonstrated that the sheath has a negligible effect on the plasma dynamics inside the quasineutral region (which accounts for the vast majority of the plasma). It is now shown that the other two assumptions made in deriving the analytic solution, namely that the plasma is quasineutral (equation (9)) and that the current density evolves slowly (equation (10)), are also well met in the reference simulation.

Considering first the quasineutral assumption, figure 11(*a*) shows a 2D plot of the quantity

$$\tilde{n} \equiv \frac{n_i - n_e}{n_i + n_e} \tag{49}$$

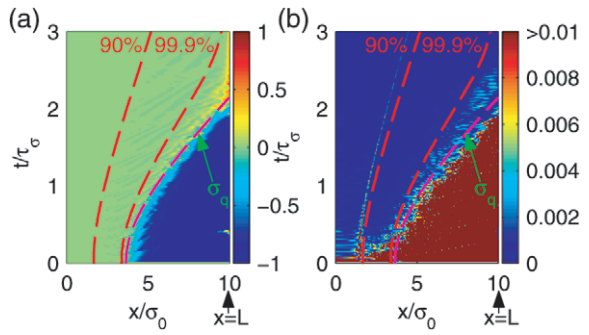


**Figure 11.** Verification that, in the reference simulation, quasineutrality is satisfied and the time evolution of the current density is sufficiently slow. $\tilde{n}$ and $|\partial\bar{j}/\partial t|$ are plotted in (*a*) and (*b*), respectively, as a function of $x/\sigma_0$ and $t/\tau_\sigma$ over the first $3\tau_\sigma$. Also plotted is the analytical prediction for the width of the quasineutral region $\sigma_q(t)$ (dashed magenta line), and the numerically derived values for lines inside which 90% and 99.9% of the electrons are contained (dashed red lines).

as a function of $x/\sigma_0$ and $t/\tau_\sigma$ for the reference simulation in the region $x \geqslant 0$. Regions where there are predominantly electrons take values $\tilde{n} \approx -1$ (blue) and regions where there are predominantly ions take values $\tilde{n} \approx 1$ (red). In neutral regions, $\tilde{n} = 0$ (green).

At $t = 0$, $\tilde{n} = 0$ everywhere. After the first time step a clearly defined quasineutral region is set up around $x = 0$. This quasineutral region is seen to expand with increasing time. At times $t \lesssim 2\tau_\sigma$, suprathermal electrons (which are sufficiently fast to overcome the confining electric field) dominate the space outside the quasineutral region, so that $\tilde{n} \approx 1$ there. These fast electrons set up a narrow (a few $\lambda_{D0}$ wide) sheath potential at the wall which attracts ions. Around time $t \approx 2\tau_\sigma$, ions begin to arrive at the boundary and dominate the density in this sheath region, so that $\tilde{n} > 0$ there (note the thin red line at the boundary for $t \gtrsim 2\tau_\sigma$).

The dashed magenta lines in figure 11 show the width of the quasineutral region as predicted by equation (45) for an unbounded expansion. Before the quasineutral region reaches the wall, this prediction is seen to match very well to the numerical simulation. This can be seen by the fact that the dashed magenta line coincides with the region where $\tilde{n}$ rapidly increases from approximately zero towards one. Once the quasineutral region reaches the wall, the plasma subsequently remains quasineutral across the entire domain except for the narrow sheath region at the wall.

Also plotted in figure 11(*a*), as dashed red lines, are the values of $x$ inside which 90% and 99.9% of the electrons are contained in the simulation. Importantly, as predicted in section 3.7, the bulk of the plasma (>99.9%) is quasineutral *at all times*. It can therefore be concluded that, except in the target sheath, the quasineutral assumption is well met in the numerical simulation, in which a value of $\lambda^*_{D0} = 10^{-2}$ was used.

In addition to the assumption of quasineutrality, it was also assumed that the rate of change of current density is small, i.e. that the quantity

$$\left|\frac{\partial\bar{j}}{\partial t}\right| \equiv \left|\frac{\partial j}{\partial t}\right| \Big/ \left|\frac{\partial}{\partial x}\int ev^2\,(Zf_i - f_e)\,\mathrm{d}v\right| \qquad (50)$$

is much less than 1 (recall equation (10)). $|\partial\bar{j}/\partial t|$ is plotted in figure 11(*b*) for the reference simulation (note that the colour scale has been cropped so that only values below 0.01 are shown). At times $t \gtrsim 0.1\tau_\sigma$, $|\partial\bar{j}/\partial t| \lesssim 0.01$ in the quasineutral region so that assumption (10) is well met. However, at earlier times $t \lesssim 0.1\tau_\sigma$, this assumption is not met because of the high values of $u_e$ compared with $u_i$ (recall figure 6). As discussed in section 4.3.2, this is due to an overly large flux of escaping suprathermal electrons for the unphysically high value of $\lambda^*_{D0} = 0.01$ in the reference simulation. Despite this, the duration and magnitude of these unphysically large currents are still small enough that quasineutrality persists once the suprathermal electrons have left the bulk plasma. The subsequent evolution of the distribution functions *inside* the quasineutral region is therefore unaffected in the reference simulation, compared with simulations with smaller (more realistic) values of $\lambda^*_{D0}$.

It is therefore concluded from this analysis that a value of $\lambda^*_{D0} = 10^{-2}$ is sufficiently small that the assumptions of quasineutrality and of negligibly small current density evolution are well met across the majority of the plasma and over the majority of times. The effect of using a lower value of $\lambda^*_{D0}$ is to decrease the initial currents caused by suprathermal electrons and, as was predicted in section 3.7, to widen the quasineutral region. The evolution of the distribution functions inside the quasineutral region are negligibly affected, however. This explains the observation by Manfredi *et al* (2011) that two simulations with $\lambda^*_{D0} = 10^{-2}$ and $\lambda^*_{D0} = 2.5 \times 10^{-3}$ behave almost identically.

### 4.6. *Effect of an alternative initial density distribution*

Until now, only a symmetrical Gaussian initial density has been considered. In this section, the effect of two alternative initial density profiles is assessed. The first is a sum of two logistic curves:

$$n_\alpha(x, t = 0) = n_{\alpha 0}\left(\frac{1}{1 + \mathrm{e}^{-(x+\sigma_0\sqrt{\frac{\pi}{2}})/s}} - \frac{1}{1 + \mathrm{e}^{-(x-\sigma_0\sqrt{\frac{\pi}{2}})/s}}\right), \qquad (51)$$

where $s$ sets the steepness of the curve and the factor $\sqrt{\pi/2}$ ensures that the total number of particles and energy remain the same as for the Gaussian case. The second is an asymmetric Gaussian distribution, with width $\sigma_0 + \sigma_0'$ for $x < 0$ and width $\sigma_0 - \sigma_0'$ for $x > 0$:

$$n_\alpha(x, t = 0) = \begin{cases} n_{\alpha 0}\exp\left(-\frac{x^2}{2(\sigma_0+\sigma_0')^2}\right) & \text{for } x < 0 \\ n_{\alpha 0}\exp\left(-\frac{x^2}{2(\sigma_0-\sigma_0')^2}\right) & \text{for } x > 0. \end{cases} \qquad (52)$$

Two simulations are discussed. The first will be referred to as the 'sigmoid simulation' with initial density given by (51), with $\sigma_0 = 0.1L$ and $s = 0.01L$. The second will be referred to as the 'asymmetric simulation' with initial density given by (52), with $\sigma_0 = 0.1L$ and $\sigma_0' = 0.03L$.

Figure 12 shows, as solid lines, the ion density evolution over the first $2\tau_\sigma$ for (*a*) the sigmoid simulation and (*b*) the

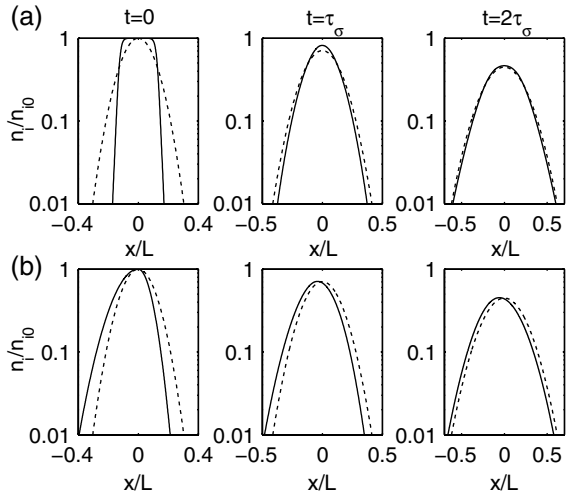


**Figure 12.** Relaxation towards the Gaussian $n_i$ profiles of the reference simulation (dotted lines) for (*a*) the sigmoid simulation and (*b*) the asymmetric simulation, both of which are plotted as solid lines.

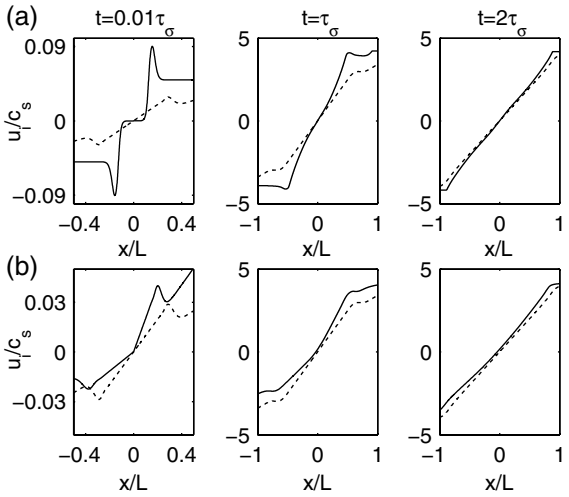


**Figure 13.** Relaxation towards the linear ion velocity profiles of the reference simulation (dotted lines) for the same two simulations plotted in figure 12.

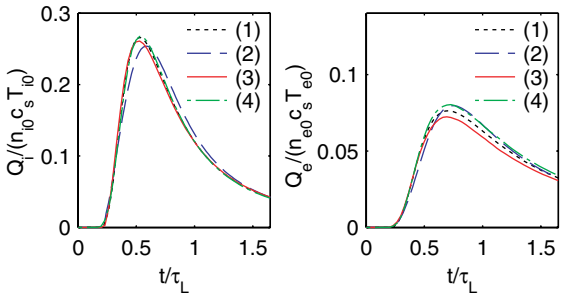


**Figure 14.** Energy flux densities to the targets due to ions (left) and electrons (right). Labelling is as follows: (1) reference simulation at $x = L$, (2) sigmoid simulation at $x = L$, (3) asymmetric simulation at $x = L$, (4) asymmetric simulation at $x = -L$.

asymmetric simulation. The evolution of the reference simulation, with $\sigma_0 = 0.1L$, is plotted as dotted lines for comparison. In both non-Gaussian simulations, the density profiles evolve towards the Gaussian profiles of the reference simulation on a timescale $\tau_\sigma$. For the asymmetric initial condition, there is a small displacement of the evolved Gaussian density away from $x = 0$, but this displacement remains constant and small throughout the expansion.

Figure 13 shows the same comparisons, but for the ion fluid velocity. At $t = 0.01\tau_\sigma$, $u_i(x)$ is considerably different in the simulations with non-Gaussian initial conditions compared with the Gaussian reference simulation. This is because, in all three simulations, $u_i$ is set by the electric field, which in turn is set by the spatial gradient of the initial density. Thus, for the sigmoid simulation (*a*), $u_i$ peaks at the edge of the plasma bunch, where the density gradient is strongest, while for the asymmetric simulation (*b*), $u_i$ is greater in the positive-$x$ region than in the negative-$x$ region, again due to the stronger initial density gradient where $x > 0$. Despite this clear difference in $u_i$ at early times, by time $t = 2\tau_\sigma$ (as was the case for the density profiles) the $u_i$ profiles for both non-Gaussian simulations are very well matched to that of the reference simulation.

Since both the density and ion velocities in the non-Gaussian simulations quickly converge to those of the Gaussian reference simulation, one would expect the energy flux densities at the target (which are dominated by the kinetic energy of the ion flow and by the convection of electron and ion perpendicular thermal energy) to also be similar to the reference simulation. This is indeed the case. Figure 14 plots $Q_i$ and $Q_e$ as a function of $t/\tau_L$ for (1) the reference simulation at $x = L$, (2) the sigmoid simulation at $x = L$, (3) the asymmetric simulation at $x = L$, and (4) the asymmetric simulation at $x = -L$. In all four cases, the energy flux densities to both targets are minimally affected by the initial density profile.

It seems, therefore, that the assumption of a Gaussian initial density makes little difference to the dynamics of the plasma expansion on timescales longer than $\tau_\sigma$. Although further work is required to understand the physical reason behind this result, it suggests that the conclusions drawn in this paper for expansion of a Gaussian plasma bunch can be extended to non-Gaussian initial density profiles as well.

### *4.7. BIT1 comparison with VESPA reference simulation*

The results presented in section 4.5 strongly suggest that a further decrease in $\lambda^*_{D0}$ will not affect the particle and energy flux densities to the target. To dispel any remaining doubt on this point, a massively parallel, collisionless BIT1 simulation was run for the same settings as the VESPA reference simulation, but with $\lambda^*_{D0} = 1.3 \times 10^{-5}$. This run required $\sim 2.5 \times 10^5$ CPU hours, spread over 4096 processors.

The results for $Q_i$ and $Q_e$ at the target according to BIT1 are plotted as solid black lines in figure 15. For comparison, the analytic solutions for $Q_i$ and $Q_e$, given by equation (34), are plotted as dotted red lines. As expected, these agree almost perfectly, legitimizing the use of an unphysically large value for $\lambda^*_{D0}$ in the VESPA simulations.

It should be noted that another BIT1 simulation was run with the target inclined to a magnetic field of magnitude such that the ion Larmor radius was $\sim$100 times longer than $\lambda_{D0}$, which is a physically realistic ratio, corresponding to a

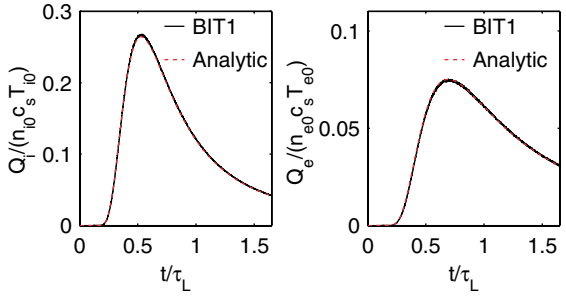


**Figure 15.** Ion and electron energy flux densities to the target calculated by a BIT1 simulation with identical input parameters to the VESPA reference simulation, except for $\lambda^*_{D0} = 1.3 \times 10^{-5}$ (solid black lines). The analytic solutions according to (34) are plotted for comparison (dotted red lines).

hydrogen plasma with $B = 1$ T, $T_{i0} = T_{e0} = 1500$ eV and $n_{e0} = 5 \times 10^{-19}$. This was found to cause oscillations in the target energy flux densities at the ion cyclotron and lower hybrid frequencies. However, once smoothed over the ion cyclotron frequency, the profiles were the same as those plotted in figure 15.

### *4.8. Effect of collisions*

Coulomb collisions were turned on in an otherwise identical BIT1 simulation to the one described above. In a collisional simulation, absolute input values become important. For this simulation, input values of $T_{e0} = 1.5$ keV, $n_{e0} = 5 \times 10^{19}$ m$^{-3}$, $\sigma_0 = 6$ m and $L = 30$ m were used. It was found that the presence of collisions allows for an isotropization between the parallel and perpendicular electron temperatures (here, the parallel temperature, which is normally labelled $T_\alpha$, will be labelled $T_\alpha^\parallel$ to distinguish it from the perpendicular temperature $T_\alpha^\perp$). Since parallel expansion causes $T_e^\parallel$ to be below $T_e^\perp$, this isotropization corresponds to an energy transfer from the perpendicular electron thermal energy to the parallel electron thermal energy.

The isotropization is demonstrated in figure 16($a$), which plots $T_e^\parallel$ (black solid lines) and $T_e^\perp$ (red solid lines) for the collisional BIT1 simulation, as well as the analytic parallel temperature given by (15) (black dotted lines), at times $t = 0.004\tau_\sigma$, $t = 0.91\tau_\sigma$ and $t = 4.49\tau_\sigma$ (note that, by time $t = 0.004\tau_\sigma$ the electric field has been set up across the quasineutral region). In the collisionless case, $T_\alpha^\perp$ remains constant in space and time at its initial value $T_{\alpha 0} = 1.5$ keV.

For times before $t \approx \tau_\sigma$, $T_e^\perp$ stays at 1.5 keV and $T_e^\parallel$ matches equation (15) inside the quasineutral region, as was also found in the collisionless case (recall figure 6). On longer timescales, however, $T_e^\perp$ drops below 1.5 keV and $T_e^\parallel$ exceeds the analytic prediction, despite the action of the sheath to decrease $T_e^\parallel$ *below* the analytic prediction. This is evidence that the perpendicular and parallel electron temperatures are beginning to isotropize. In contrast to the electrons, figure 16($b$) shows that very little isotropization occurs between the ion temperatures so that $T_i^\parallel$ and $T_i^\perp$ correspond very well to the collisionless case within the quasineutral region.

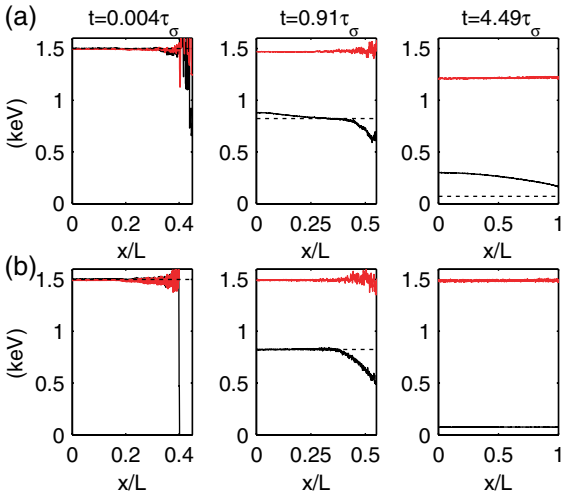


**Figure 16.** Electron temperature isotropization in the collisional BIT1 simulation. ($a$) $T_e^\parallel$ (black solid lines) and $T_e^\perp$ (red solid lines) in the simulation, compared with equation (15) (black dotted lines) at different times as indicated. ($b$) The same plot for the ion temperatures.

The increased mobility of the electrons in the parallel direction due to electron temperature isotropization causes an increase in the magnitude of the electric field, which in turn accelerates the ions to higher fluid velocities than in the collisionless case. This is demonstrated in figure 17, in which solid lines represent ($a$) $e\phi(x)/T_{e0}$ and ($b$) $u_i(x)/c_s$ for the collisional simulation, at the same times that were plotted in figure 16. These should be compared with the dotted lines, which represent the collisionless analytic predictions of equations (17) and (13) (note that the analytic $\phi$ has been normalized to have the same peak value as the BIT1 simulation). As was the case for the temperatures, before $t \approx \tau_\sigma$, $\phi$ and $u_i$ agree well with the collisionless case in the quasineutral region. On longer timescales, however, both $|\partial\phi/\partial x|$ and $u_i$ are significantly increased compared with the collisionless case (the noisy values at $t = 0.004\tau_\sigma$ are due to the particle-in-cell nature of BIT1).

Figure 18 compares the resulting ion and electron energy flux densities at the target with the collisionless analytic equation (35). The increase in $u_i$ at the target, which occurs before $Q_i$ reaches its peak, acts to increase the peak value of $Q_i$ compared with the collisionless case. The drop in $T_e^\perp$ decreases the convected electron thermal energy (and therefore $Q_e$) compared with the collisionless case; however, the peak $Q_{tot}$ is still increased. Thus, for the particular input parameters used in this collisional BIT1 simulation, electron–electron collisions do have a role to play. They act to transfer energy from the perpendicular plane to the parallel direction, thereby increasing the electric field and accelerating the ions more than in the collisionless case. This results in a ~25% increase in the peak value of $Q_{tot}$ compared with the collisionless case.

It is important to estimate the strength of this isotropization effect for different input parameters. The isotropization time for species $\alpha$ is given by (NRL Plasma Formulary)

$$\tau_T^\alpha = \frac{m_\alpha^{1/2}(kT_\alpha^\parallel)^{3/2}}{2\pi q_\alpha^4 n_\alpha \ln\Lambda} A^2 \left(-3 + (A+3)\frac{\tan^{-1}\left(A^{1/2}\right)}{A^{1/2}}\right)^{-1}, \quad (53)$$

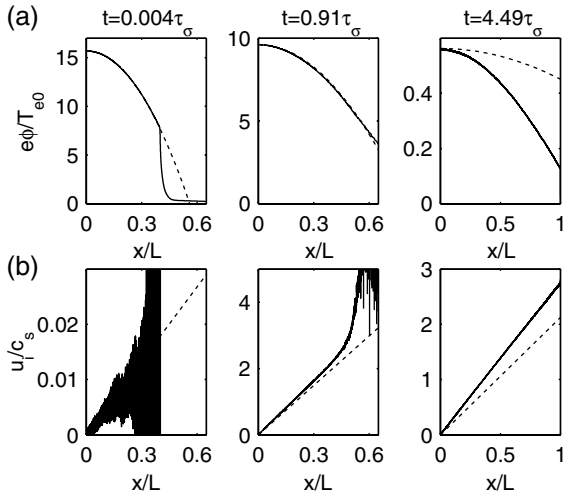


**Figure 17.** Effect of electron temperature isotropization on (*a*) $e\phi(x)/T_{e0}$ and (*b*) $u_i(x)/c_s$. The same times are plotted as in figure 16. Solid lines represent the collisional BIT1 simulation and dotted lines represent the collisionless analytic solutions from equations (17) and (13). In (*a*), the analytic $\phi$ has been normalized to have the same peak value as the BIT1 simulation.

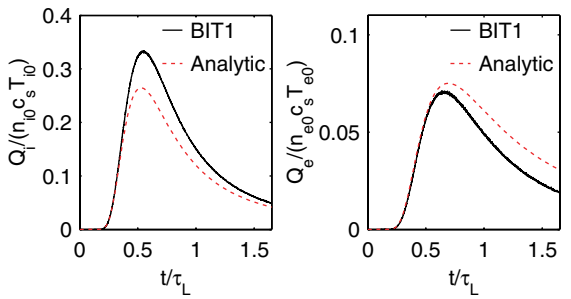


**Figure 18.** Effect of collisions on the ion and electron energy flux densities in the BIT1 simulation.

where $\ln\Lambda$ is the Coulomb logarithm and $A \equiv T_e^{\perp}/T_e^{\parallel} - 1$ (note that for the case considered here $A > 0$). It is seen that $\tau_T^i/\tau_T^e = \sqrt{m_i/m_e}$, i.e. isotropization between ion temperatures takes much longer than between electron temperatures, in agreement with the collisional BIT1 simulation. Electron temperature isotropization is expected to be significant if it has time to occur before the energy flux density to the target reaches its peak, i.e. if $\tau_T^e < t_Q^{max}(L) = 0.556L/c_s$.

A representative value for $\tau_T^e$ can be calculated using the collisionless values for $T_e^{\parallel}$, $T_e^{\perp}$ and the peak $n_e$, when $t = t_Q^{max}(L)$. The resulting ratio of $\tau_T^e/t_Q^{max}(L)$ is plotted in figure 19 as a function of $T_{e0}$, for different combinations of $\sigma_0$ and $L$, and for a density corresponding to the ITER pedestal density of $8 \times 10^{19}\,m^{-3}$. These values should be compared with the value of $\tau_T^e/t_Q^{max}(L)$ in the collisional BIT1 simulation, which was 0.46 and is shown as a dotted line. If values fall below this line then isotropization is expected to play a more important role than in the BIT1 simulation.

For values of $L$ equal to to a typical equilibrium connection length of $L \sim 60\,m$ on ITER, $\tau_T^e/t_Q^{max}(L)$ is seen to be larger than the BIT1 collisional simulation for realistic (pedestal) values of $T_{e0}$ and for $\sigma_0 \gtrsim 6\,m$. Thus, electron temperature

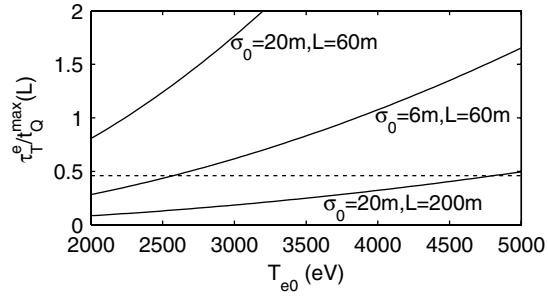


**Figure 19.** Expected strength of the electron temperature isotropization effect (measured by $\tau_T^e/t_Q^{max}(L)$) as a function of $T_{e0}$ for $n_{e0} = 8 \times 10^{19}\,m^{-3}$ and for different values of $\sigma_0$ and $L$, as indicated. The dotted line shows the value of $\tau_T^e/t_Q^{max}(L)$ for the collisional BIT1 simulation.

isotropization is expected to play less of a role than reported for the BIT1 simulation described above. However, if the connection length is significantly longer than its equilibrium value (as shown by the $\sigma_0 = 20\,m$, $L = 200\,m$ case), then isotropization will have more time to take place, and the total energy flux density would be expected to peak at a significantly higher value than for the collisionless case. It is concluded that the absolute values of $L$ and $\sigma_0$ during an ELM on ITER will set the degree to which electron isotropization (and the resulting increase in peak $Q_{tot}$) are important.

### *4.9. Effect of a distributed source in time*

Until now, the source function has been instantaneous. In reality, however, the duration of the source may be significant compared with $\tau_\sigma$, and possibly compared with the longer time $\tau_L$ also. A preliminary investigation into the effect of setting $\tau_{src} > 0$ is made in this section. It is important to note that, as for the instantaneous-source case, the dynamics inside the quasineutral region, as well as the particle and energy flux densities at the target, were found to be independent of $\lambda_{D0}^*$ for $\lambda_{D0}^* \lesssim 10^{-2}$. This allowed the simulations to be completed on reasonable timescales. For all simulations in this section, a value of $\lambda_{D0} = 10^{-2}$ was used.

*4.9.1. Upstream evolution is independent of the connection length.* When $\tau_{src}$ takes finite values, the upstream density $n_\alpha(x = 0)$ no longer peaks at $t = 0$ with a value $n_{\alpha 0}$. Instead, $n_\alpha(x = 0)$ peaks at $t = \tau_{src}$ with a value that is lower than $n_{\alpha 0}$ and which decreases with increasing $\tau_{src}$. This is demonstrated in figure 20, which plots $n_e(x = 0)$ as a function of $t/\tau_\sigma$, for different values of $\tau_{src}$ and $L^*$. As expected for the $\tau_{src} \to 0$ cases (plotted in black), the evolution of $n_\alpha(x = 0)$ is independent of the connection length for the explored parameter range. This implies that the sheath has no effect on the upstream density evolution, at least for $L^* \geqslant 2$. Importantly, this lack of dependence on the connection length is also seen for finite values of $\tau_{src}$ (plotted in green, blue and red for different values of $\tau_{src}$). Thus, the sheath plays little role in the upstream density evolution even when the source is finite. Rather, the evolution is determined by $\tau_{src}/\tau_\sigma$.

Consider now the evolution of the upstream temperature $T_\alpha(x = 0)$. This is shown in figure 21 for the same set of

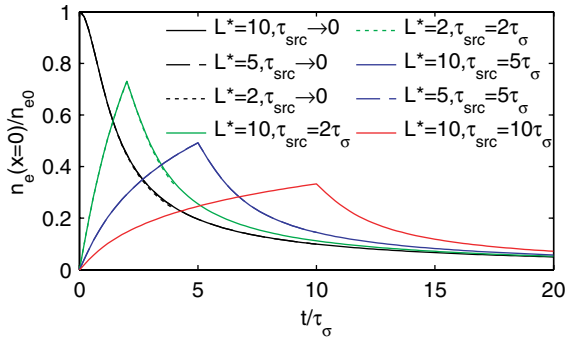


**Figure 20.** Evolution of $n_e(x=0)/n_{e0}$ for different values of $\tau_{src}$ and $L^*$, as indicated.

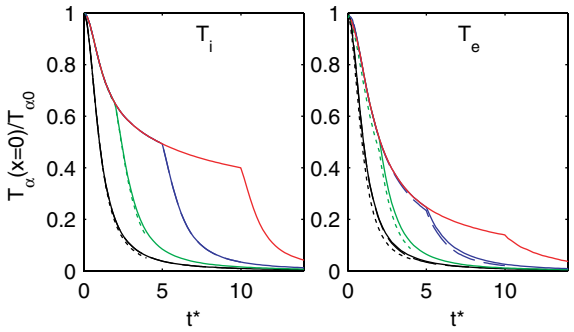


**Figure 21.** Evolution of $T_i(x=0)/T_{i0}$ and $T_e(x=0)/T_{e0}$ for different values of $\tau_{src}$ and $L^*$, as indicated. The same line styles are used as in figure 20.

simulations that were plotted in figure 20 (note that the same line styles and colours are used). As for the upstream density, the upstream temperature evolution is determined primarily by $\tau_{src}/\tau_\sigma$. The connection length does play some role (there is a small decrease in $T_e(x=0)$ for small $L^*=2$, compared with higher values of $L^*$, due to the action of the sheath), but this effect is minimal. Note that, before the source is removed, the fall in $T_\alpha(x=0)$ is identical for all values of $\tau_{src}/\tau_\sigma$. Furthermore, $T_e(x=0)$ is seen to decrease faster than $T_i(x=0)$ while the source is present. This is due to the transferral of energy from electrons to ions via the potential created by a spatial gradient in the ELM source. It is not due to the target sheath.

*4.9.2. Target $Q_{tot}$ deviates from $\sigma_0 \to 0$ solution when $\tau_{src}/\tau_L \gtrsim 0.1$.* Although the upstream evolution with a finite source duration is determined by $\tau_{src}/\tau_\sigma$, the target evolution of the total target energy flux density is determined by $\tau_{src}/\tau_L$. Figure 22 plots $Q_{tot}$ at the target for different values of $\tau_{src}$ and for $L^*=10$. As long as $\tau_{src} \lesssim 0.1\tau_L$, the evolution of the target energy flux density remains almost unchanged from the $\tau_{src} \to 0$ case.

*4.9.3. Electron heat flux densities are no longer negligible.* Consider the particular simulation with the same input parameters as the reference simulation, but with $\tau_{src}=10\tau_\sigma=\tau_L$ (the red lines in figures 20 and 21). Figure 23 plots the total energy flux densities (solid lines) and the heat flux

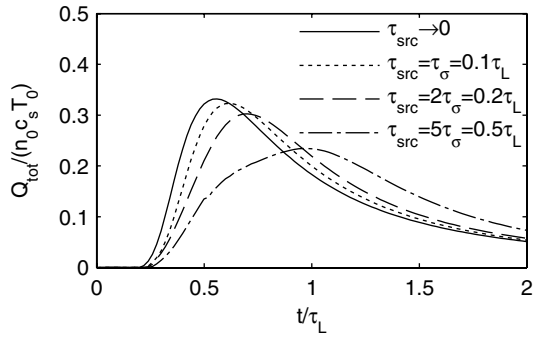


**Figure 22.** $Q_{tot}/(n_{e0}c_sT_{e0})$ at the target for different values of $\tau_{src}$ and for $L^*=10$.

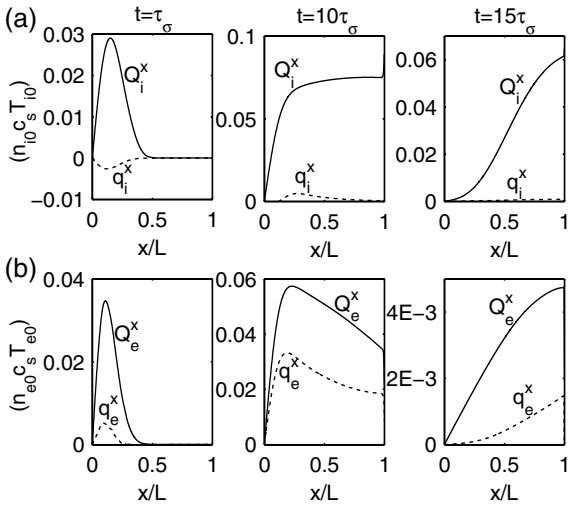


**Figure 23.** $Q_\alpha$ (solid lines) and $q_\alpha$ (dotted lines) for ($a$) ions and ($b$) electrons in a simulation equivalent to the reference simulation, but with $\tau_{src}=10\tau_\sigma=\tau_L$. Plots are made at times spanning the expansion, as indicated.

densities (dotted lines) for ($a$) ions and ($b$) electrons, at $t=\tau_\sigma$, $t=10\tau_\sigma=\tau_{src}$ and at $t=15\tau_\sigma$.

It is seen that $q_e^x$ makes a significant contribution to $Q_e^x$ throughout the expansion. In fact, with a time-distributed source, the ion and electron distribution functions are strongly non-Maxwellian, and are not symmetric about the fluid velocity. The underlying physics for this difference between the instantaneous and time-distributed source cases is still under investigation. Although not fully understood, the resulting finite electron heat flux density has important consequences for the validity of using a fluid approach to model the expansion with a time-distributed source. In particular, it is expected that the accuracy of a fluid closure which sets $q_\alpha^x=0$ will be significantly diminished compared with the instantaneous-source case.

*4.9.4. The target sheath is still negligible.* For the instantaneous source, it was observed that the effect of a target sheath at $x=L$ can be eliminated in the simulation by moving the boundary to $x=2L$. Assuming that this is also true for finite values of $\tau_{src}$, the same exercise can be carried out to determine the role of the sheath when $\tau_{src}>0$. Figure 24 shows the simulation values for $Q_i^x$ ($a$), $Q_e^x$ ($b$) and $Q_e+Q_i$

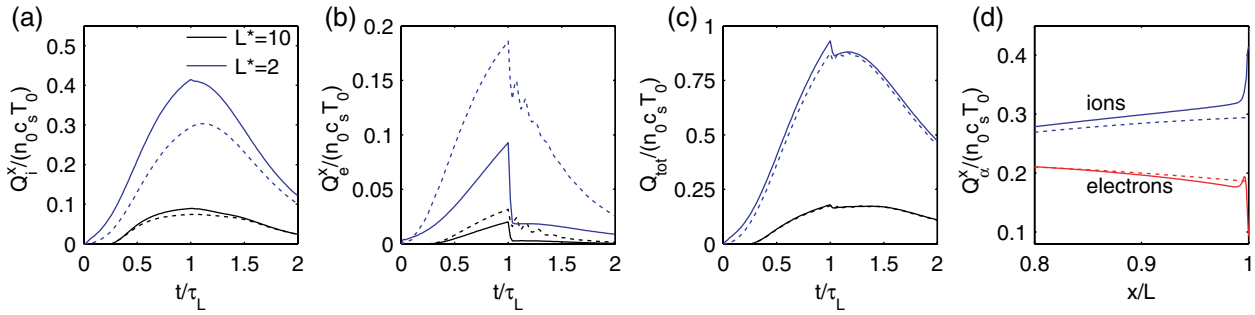


**Figure 24.** Effect of the sheath on target energy flux densities, when $\tau_{src} = \tau_L$, for $L^* = 10$ and $L^* = 2$. (*a*)–(*c*) Energy flux densities at the target. (*d*) $Q_e^x$ and $Q_i^x$ as a function of $x/L$ at time $t = \tau_{src}$ for the $L^* = 2$ simulation. In all plots, solid lines represent results with a boundary at $x = L$ and dotted lines represent results with the boundary moved to $x = 2L$.

(*c*) at the target for simulations with $L^* = 10$ (black lines) and $L^* = 2$ (blue lines). Values of $Q_\alpha^x$ as a function of $x/L$ at time $t = \tau_{src}$ are plotted for the $L^* = 2$ simulation in (*d*).

For both values of $L^*$, $Q_e^x$ makes a larger contribution to $Q_{tot}$ than in their equivalent instantaneous-source cases (recall figure 9). However, the contribution is still small, due to energy transferral from electrons to ions via the electric field. For the $L^* = 10$ simulation, moving the boundary to $x = 2L$ makes little difference to either $Q_i^x$ or $Q_e^x$ at the target, and makes almost no difference to $Q_{tot}$. It is concluded that the sheath has little effect at this value of $L^*$. For $L^* = 2$, the sheath does act to transfer energy from electrons to ions within the sheath region, as it did in the instantaneous-source simulation with the same value of $L^*$ (recall figure 9). However, also consistent with that instantaneous-source simulation is the fact that $Q_{tot}$ at the target is almost completely unaffected by moving the boundary. Furthermore, as is seen in figure 24(*d*), away from the sheath entrance $Q_\alpha^x$ is almost unaffected by moving the boundary to $x = 2L$. The majority of the difference between $Q_\alpha^x$ at the target in the simulation with a boundary at $x = L$ and $Q_\alpha^x$ at the target in the simulation with boundary at $x = 2L$ arises due to energy transfer which takes place inside the sheath. Thus, the sheath acts only to alter the partition of ion and electron energies reaching the target, but does not affect the dynamics of the plasma expansion to the target.

## 5. Discussion

### *5.1. Estimation of realistic input parameters for an ELM filament*

*5.1.1. $m^*(\equiv m_i/m_e)$ and $Z$.* These inputs are straightforward. Assuming pure hydrogen, deuterium and helium plasmas, the mass ratios are $m^* = 1836$, $m^* = 3672$ and $m^* = 7294$, respectively, and the proton numbers are $Z = 1$, $Z = 1$, $Z = 2$.

*5.1.2. $T^*(\equiv T_{i0}/T_{e0})$.* Direct measurements for temperature ratios during an ELM do not exist. However, the injected temperature ratio is presumably similar to its value at the inter-ELM pedestal, i.e. $T^* \sim$ 1–3 (see Kočan *et al* (2011) and references therein).

*5.1.3. $\sigma_0$.* Although not an input parameter itself, the remaining three dimensionless inputs ($\lambda^*_{D0}$, $L^*$ and $\tau^*_{src}$) require knowledge of the parallel extent of the filament, $\sigma_0$. It is known from double-null experiments that the ELM pressure perturbation occupies a region on the outboard side only (Counsell *et al* 2002, Petrie *et al* 2003). Furthermore, at least in the upstream region, the filament appears to remain aligned to the pre-ELM magnetic field lines (Kirk *et al* 2006, Jakubowski *et al* 2009). Assuming that the perturbation occupies a similar poloidal extent to the ballooning region of the particle flux in L-mode, measured as $\theta_0 \sim 0.5$ rad on Tore Supra (Gunn *et al* 2007), $\sigma_0$ can be estimated as

$$\sigma_0 \sim R\theta_0 q_{95} \sim 0.5 R q_{95}, \tag{54}$$

where $q_{95}$ is the edge safety factor. For ITER with $q_{95} = 3$ and $R = 6.2$ m, (54) gives $\sigma_0 \sim 9$ m. It should be noted that fast camera images on MAST show the density perturbations to be more spread out in the parallel direction than this number suggests (Kirk *et al* 2006). This may be because significant parallel transport has occurred before the filaments are imaged, although further investigation is required on this point.

*5.1.4. $\lambda^*_{D0}(\equiv \lambda_{D0}/\sigma_0)$.* $\lambda_{D0} = \sqrt{\varepsilon_0 T_{e0}/e^2 n_{e0}}$ requires typical values for $T_{e0}$ and $n_{e0}$. $T_{e0}$ is assumed to be the pedestal electron temperature, expected to be ~4.3 keV for $Q_{DT} = 10$ conditions on ITER (Loarte *et al* 2004). The peak density of a filament is typically measured as being similar to the pedestal density (Loarte *et al* 2003, Kirk *et al* 2006, Beurskens *et al* 2009), i.e. $\sim 8 \times 10^{19}$ m$^{-3}$ for a $Q_{DT} = 10$ ITER plasma (Loarte *et al* 2004). Using $T_{e0} = 4.3$ keV, $n_{e0} = 8 \times 10^{19}$ m$^{-3}$ and $\sigma_0 = 9$ m gives $\lambda^*_{D0} = 6 \times 10^{-6}$ on ITER, and values to within an order of magnitude for all other machines. An important conclusion from this paper is that the particle and energy flux densities to the target are independent of $\lambda^*_{D0}$ as long as $\lambda^*_{D0} \lesssim 10^{-2}$. This condition is clearly met in experiment (note that, for a time-distributed source, $n_{e0}$ might be up to ~3 times larger than the measured peak density, but this will only act to decrease $\lambda^*_{D0}$ further).

*5.1.5. $L^*(\equiv L/\sigma_0)$.* If the magnetic field lines within the filament remain unperturbed relative to their pre-ELM state, then the connection length within the filament can be estimated as $L \approx \pi R q_{95}$. Using (54) gives $L^* \sim \pi/\theta_0$ and is machine

independent. With $\theta_0 = 0.5$ rad, this gives $L^* \sim 6$. Even if the source was spread over a poloidal angle of $\theta_0 = 90°$, $L^*$ would still only go down to ~2. Furthermore, in reality the connection lengths within an ELM filament may be significantly increased compared with their pre-ELM values, with the majority of the field line existing in the X-point region. JOREK simulations, for example, suggest perturbed connection lengths during the ELM phase of up to $\sim 17\pi Rq_{95}$ on JET (Huysmans *et al* 2009). It seems likely, therefore, that the result from this paper that the sheath only plays a role when $L^* \lesssim 5$, and that even at $L^* = 2$ it only acts to repartition energy between ions and electrons (not to alter the total energy flux density to the target), is physically relevant on all machines.

Note that this result is unlikely to be significantly affected if the source is centred away from $x = 0$, or if the injected particles are given an initial drift velocity towards one of the targets. As long as the majority of electrons have time to cool before the bulk of the plasma reaches the target, the sheath is expected to be negligible.

*5.1.6.* $\tau_{\rm src}$. An absolute value for $\tau_{\rm src}$ is particularly difficult to estimate, since it depends on how the pressure perturbation in the filament becomes magnetically connected to the target. If it is the case that the filament drifts radially across relatively static field lines and into the pre-ELM SOL, then the modelled field lines are those of the pre-ELM SOL and $\tau_{\rm src}$ is the time required for the filament to transport into it. This is the so-called 'drift hydrodynamic' transport proposed in (Fundamenski *et al* 2007). $\tau_{\rm src}$ can then be estimated as $\tau_{\rm src} \approx \delta_r/u_r$, where $\delta_r$ is the radial extent of the filament and $u_r$ is the average radial speed of the filament. On the other hand, if it is the case that the filament becomes magnetically connected to the target due to the motion of field lines, so that the filament serves as a conduit for the pedestal energy (Kirk *et al* 2006), then the modelled field lines *are* those moving field lines and $\tau_{\rm src}$ is a combination of the time required for the filament to form and the time for which the field lines are connected to the pedestal. In this case, $\tau_{\rm src}$ is more difficult to estimate. Resolving which of these two models best fits reality should be a primary focus of the ELM transport community. For now, however, a direct determination of the absolute value for $\tau_{\rm src}$ remains elusive.

That being said, there does appear to be strong experimental evidence that, whichever model is more realistic, $\tau_{\rm src} \lesssim 0.1\tau_L$. This comes primarily from the excellent agreement that is found between the free-streaming model and experiment. In (Eich *et al* 2009) the power flux density to the target predicted by the free-streaming model (essentially equation (34)) was compared with the total power arriving at the target according to infra-red camera measurements on JET and ASDEX Upgrade. An excellent fit to the absolute measurements at the outer target in normal field configuration was achieved when values of $L \approx 9\pi Rq_{95}$ were used for both JET and ASDEX Upgrade measurements. The results of this paper suggest that this agreement between equation (34) and experiment can only exist if $L^* \gtrsim 5$ and $\tau_{\rm src} \lesssim 0.1\tau_L$. Furthermore, the free-streaming model predicts that the rise time for the total power to the target should be directly proportional to $L/c_{\rm s}$ (recall equation (36)) and, using $L \propto Rq_{95}$, this is indeed what is found in experiment across a wide range of $R$, $q_{95}$ and $c_{\rm s}$ (Loarte *et al* 2004, Loarte *et al* 2007).

As discussed by Eich *et al* (2009), the excellent agreement between (34) and experiment *could* also be recovered if a source with duration several times longer than $\tau_L$ was used, and if the connection length remained unperturbed from its pre-ELM value. However, such a source would have to vary in time in just such a way that the power to the target mimics the free-streaming time profile. It would have to do this on multiple machines *and* it would have to vary with $L$ and $c_{\rm s}$ in just such a way that the observed proportionality between the rise time and $L/c_{\rm s}$ is maintained. Given these stringent conditions, it seems more likely that $L^* \gtrsim 5$ and $\tau_{\rm src} \lesssim 0.1\tau_L$.

An objection to the suggestion that $\tau_{\rm src} \lesssim 0.1\tau_L$ might be that the total energy reaching the target cannot be accounted for unless the upstream density rises to values which are considerably higher than observed in experiment. However, this is not necessarily the case, since the reduction in upstream density due to a distributed source is dependent on the value of $\tau_{\rm src}$ relative to $\tau_\sigma$, *not* relative to $\tau_L$ (section 4.9.1). For large values of $L^*$, it can be the case that $\tau_{\rm src} \lesssim 0.1\tau_L$ whilst at the same time $\tau_{\rm src}$ significantly exceeds $\tau_\sigma$. For example, using (54) for $\sigma_0$ and the experimentally fitted value of $L \approx 9\pi Rq_{95}$ gives $L^* \sim 9\pi/\theta_0$. A source duration of $0.1\tau_L$ will then be equivalent to $0.9\pi/\theta_0\tau_\sigma = 5.7\tau_\sigma$ for $\theta_0 = 0.5$ rad. Interpolating the peak values in figure 20, this source duration, along with a peak upstream electron density of $5 \times 10^{19}$ m$^{-3}$, corresponds to a value of $n_{\rm e0} = 10.7 \times 10^{19}$ m$^{-3}$. The total energy in the ELM is then given by

$$E_{\rm ELM} \approx 3n_{\rm fil}A_\perp(E_{\rm e0} + E_{\rm i0}), \tag{55}$$

where $n_{\rm fil}$ is the number of filaments and $A_\perp$ is the area of a single filament in the drift plane. On JET, $n_{\rm fil} \sim$ 10–20 (Pitts *et al* 2006, Jakubowski *et al* 2009). The perpendicular area of a filament is roughly elliptical, with a major radius in the diamagnetic direction of $\delta_\wedge \sim$ 10–20 cm and minor radius in the radial direction of $\delta_r \sim$ 4–5 cm (Kirk *et al* 2008) and references therein). Thus, $A_\perp \approx \pi\delta_\wedge\delta_r \sim$ 30–80 cm$^2$. Using $T_{\rm e0} = 1500$ eV and $T^* = 3$ gives an upper range for $E_{\rm ELM}$ of 320 kJ, in line with typical experimental measurements on JET (Beurskens *et al* 2009).

### *5.2. Can a fluid approach be used to model parallel ELM transport?*

This is an important question for the edge plasma modelling community since many codes, such as EDGE2D and JOREK, use a fluid approach to model ELM parallel transport (Wiesen *et al* 2011, Pamela *et al* 2011). It might be inferred from the low collisionality of the pedestal, that fluid equations, which assume a high collisionality, are not appropriate. However, high collisionality is a sufficient, but not a necessary, condition for a fluid approach to be valid. If the velocity distribution functions remain symmetric about the fluid velocity then there is no heat flux density and the fluid equations can be closed

by setting $q_\alpha = 0$. The simulations presented in this paper show that with an instantaneous source this is indeed the case inside the quasineutral region of a plasma bunch expanding into vacuum.

In fact, since the temperatures are constant in space for the adiabatic expansion of a quasineutral Gaussian plasma bunch into infinite vacuum, analytic solutions to the fluid equations can be derived with the assumptions that $n_e = n_i$, $T_\alpha =$ constant and $q_\alpha = 0$ (Mora 2005). Actually, the solution given by Mora (2005) assumed cold ions; however, the inclusion of warm ions using the same procedure described in that reference is trivial. These solutions for $n_\alpha$, $u$ and $T_\alpha$ are then identical to those given in section 3.2 by solving the VP equations. In this particular case, therefore, the fluid approach is exact. The only 'kinetic aspect' to the expansion comes outside the quasineutral region, and is of negligible consequence for the particle and energy flux densities to the wall.

It was shown in section 4.6 that, for an instantaneous source, the solution on timescales longer than $\tau_\sigma$ is fairly insensitive to the initial shape of the density perturbation. However, it remains to be seen whether this is also the case when a fluid model is used. In addition, the transfer of energy from the perpendicular to parallel directions, demonstrated in section 4.8, would not be captured in typical fluid models which assume a single temperature for electrons and ions. Another important aspect not discussed in this paper is the effect of a background plasma on the expansion dynamics. Whether a background plasma affects kinetic and fluid simulations in the same way will be investigated in future work. Finally, as was shown in section 4.9.3, when $\tau_{src} \gtrsim \tau_\sigma$, a significant electron heat flux density arises. A fluid closure which sets $q_e = 0$ may lead to significant error in this case, and this should be a topic of future research. This can be seen as a continuation of the work started by Havlíčková *et al* (2012).

The results from this paper have important implications for the boundary conditions that should be used in fluid simulations of ELM filaments, which are only able to model up to the sheath entrance. In general, when $L^* \gtrsim 5$, the plasma behaves as if there was a negligible sheath. Such a situation might best be modelled using continuous gradient boundary conditions, although this requires further investigation. Certainly, use of the marginal Bohm criterion $M = 1$ cannot be justified, since the Mach number at the sheath entrance can significantly exceed unity during the ELM transient. Furthermore, although it may be reasonable in the steady state to set the energy flux densities at the sheath entrance such that $Q_i^x = \gamma_i n_i T_i c_s^{se}$ and $Q_e^x = \gamma_e n_e T_i c_s^{se}$ (where $c_s^{se}$ is the local sound speed at the sheath entrance and $\gamma_i \approx 3.5$ and $\gamma_e \approx 5$ are the sheath transmission coefficients), this is not justifiable during an ELM transient, particularly for the dominant ion energy flux density. To see this, consider the instantaneous-source case. For $L^* = 2$, $Q_i^x$ peaks at a value equal to $5.1 n_i T_i c_s^t$, in reasonable agreement with the standard boundary condition. However, for $L^* = 10$, $Q_i^x$ peaks at a value equal to $956 n_i T_i c_s^t$, well in excess of the value given by the steady-state boundary condition. Such boundary conditions are therefore inadvisable.

## 6. Conclusions

This work has introduced an existing analytic solution for plasma expansion to the ELM transport community. The solution solves the VP model for the collisionless, adiabatic expansion of a Gaussian density perturbation into an infinite vacuum, assuming quasineutrality at all times. In the limit $\sigma_0 \to 0$, the solution recovers the free-streaming solution once a substitution $v_{Ti} \to c_s$ is made. Furthermore, as long as $L^* \gtrsim 5$, the free-streaming solution for the particle and energy flux densities at the target are a good approximation to those found for the general $L^*$ case. This helps one to explain how the free-streaming model can agree so well with measured target power loads, and suggests that $L^* \gtrsim 5$ and $\tau_{src}/\tau_L \lesssim 0.1$ in experiment. It was also demonstrated, via a comparison with numerical solutions, that if the plasma is quasineutral in the bulk initially, then it is quasineutral in the bulk at all times.

For values of $L^*$ down to the minimum explored value of $L^* = 2$, the dynamics of the expansion inside the quasineutral region is unaffected by the presence of a target sheath. The target sheath is negligible because the majority of electrons, which arrive with the ions, are too cold to set up a significant sheath by the time they reach the target. For $L^* \gtrsim 5$ the electron and ion energy flux densities at the target are negligibly affected by the formation of this weak sheath. Energy exchange from electrons to ions occurs on a timescale $\tau_\sigma$ via a potential which is set up due to the parallel gradient in the density, and has nothing to do with the target sheath. For $L^* \lesssim 5$ the sheath does act to repartition the target energy flux density between electrons and ions, but the *total* target energy flux density is unaltered from the analytic solution which ignores the sheath. Furthermore, numerical simulations suggest that the sheath can also be neglected when the source is spread over a significant duration, up to $\tau_{src} = \tau_L$.

This conclusion is in contrast to the existing consensus in the ELM parallel transport community. In the ITER Physics Basis (Loarte *et al* 2007), for example, it was stated that the 'sheath plays a major role in limiting the energy flux from the pedestal plasma to the divertor during the ELM power pulse'. The evidence in this paper suggests that in fact sheath formation can be ignored, as long as $L^* \gtrsim 5$.

For the particular case of an adiabatic expansion of a Gaussian density perturbation into an infinite vacuum, the fluid approach is exact. Future work will investigate the agreement between fluid and kinetic models for a time-distributed source and in the presence of a background plasma. Also, further complexity will be introduced to the VESPA simulations by including magnetic mirroring effects and collisions.

## Acknowledgments

This work was supported by the European Community under the contract of Association between EURATOM, CEA and the French Research Federation for Fusion Study. The views and opinions expressed herein do not necessarily reflect those of the European Commission. BIT1 simulations were carried out using the HELIOS supercomputer system at Computational Situational Centre of International Fusion

Energy Research Centre (IFERC-CSC), Aomori, Japan, under the Broader Approach collaboration between Euratom and Japan, implemented by Fusion for Energy and JAEA. D Tskhakaya acknowledges support by the projects P21941-N16 and ST09-269-4-140.



## References

Bécoulet M *et al* 2003 *Plasma Phys. Control. Fusion* **45** A93
Beurskens M N A *et al* 2009 *Nucl. Fusion* **49** 125006
Counsell G *et al* 2002 *Plasma Phys. Control. Fusion* **44** 827
Dorozhkina D S and Semenov V E 1998 *Phys. Rev. Lett.* **81** 2691
Dorozhkina D S and Semenov V E 1999 *J. Exp. Theor. Phys.* **89** 468
Eich T *et al* 2009 *J. Nucl. Mater.* **390–391** 760
Fundamenski W *et al* 2006 *Plasma Phys. Control. Fusion* **48** 109
Fundamenski W *et al* 2007 *Plasma Phys. Control. Fusion* **49** R43
Gunn J P *et al* 2007 *J. Nucl. Mater.* **363–365** 484
Havlíčková E *et al* 2012 *Plasma Phys. Control. Fusion* **54** 045002
Jachmich S *et al* 2011 *J. Nucl. Mater.* **415** S894
Jakubowski M W *et al* 2009 *J. Nucl. Mater.* **390–391** 781
Huysmans G T A *et al* 2009 *Plasma Phys. Control. Fusion* **51** 124012
Kirk A *et al* 2005 *Plasma Phys. Control. Fusion* **47** 315
Kirk A *et al* 2006 *Phys. Rev. Lett.* **96** 185001
Kirk A *et al* 2008 *J. Phys. Conf. Ser.* **123** 012011
Kočan *et al* 2011 *J. Nucl. Mater.* **415** S1133
Kovalev V *et al* 2002 *J. Exp. Theor. Phys.* **95** 226
Kovalev V and Bychenkov V *et al* 2003 *Phys. Rev. Lett.* **90** 185004
Loarte A *et al* 2003 *Plasma Phys. Control. Fusion* **45** 1549
Loarte A *et al* 2004 *Phys. Plasmas* **11** 2668
Loarte A *et al* 2007 *Nucl. Fusion* **47** S203
Manfredi G *et al* 1993 *Phys. Fluids* B **5** 388
Manfredi G *et al* 2011 *Plasma Phys. Control. Fusion* **53** 015012
Mora P 2005 *Phys. Plasmas* **12** 112102
NRL Plasma Formulary, NRL/PV/6790-98-358
Pamela S J P *et al* 2011 *Plasma Phys. Control. Fusion* **53** 054014
Petrie T W *et al* 2003 *Nucl. Fusion* **43** 910
Pitts R A *et al* 2006 *Nucl. Fusion* **46** 82
Snyder P B and Wilson H R 2003 *Plasma Phys. Control. Fusion* **45** 1671
Stangeby P C 2000 *The Plasma Boundary of Magnetic Fusion Devices* (Bristol: Institute of Physics Publishing)
Tskhakaya D and Schneider R 2007 *J. Comput. Phys.* **225** 829
Tskhakaya D *et al* 2008 *Contrib. Plasma Phys.* **48** 121
Tskhakaya D *et al* 2009 *J. Nucl. Mater.* **390–391** 335
Valluri S R *et al* 2000 *Can. J. Phys* **78** 823
Wiesen S *et al* 2011 *Plasma Phys. Control. Fusion* **53** 124039